

# Triplet Excitation-Energy Transfer Couplings from Subsystem Time-Dependent Density-Functional Theory

Sabine Käfer,<sup>†</sup> Niklas Niemeyer,<sup>†</sup> Johannes Tölle,<sup>‡</sup> and Johannes Neugebauer<sup>\*,†</sup>

*<sup>†</sup>University of Münster, Organisch-Chemisches Institut  
and Center for Multiscale Theory and Computation,  
Corrensstraße 36, 48149 Münster, Germany*

*<sup>‡</sup>Division of Chemistry and Chemical Engineering,  
California Institute of Technology, Pasadena, California 91125, USA*

E-mail: j.neugebauer@uni-muenster.de

Date: December 12, 2023

## Abstract

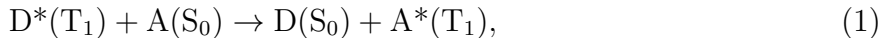
We present an implementation of Triplet Excitation-Energy Transfer (TEET) couplings based on subsystem-based Time-Dependent Density-Functional Theory (sTDDFT). TEET couplings are systematically investigated by comparing “exact” and approximate variants of sTDDFT. We demonstrate that, while sTDDFT utilizing explicit approximate Non-Additive Kinetic Energy (NAKE) density functionals is well-suited for describing Singlet Excitation-Energy Transfer (SEET) processes, it is inadequate for characterizing TEET. However, we show that Projection-based Embedding (PbE)-based sTDDFT addresses the challenges faced by NAKE-sTDDFT and emerges as a promising method for accurately describing electronic couplings in TEET processes.

We also introduce the mixed PbE-/NAKE-embedding procedure to investigate TEET effects in solvated pairs of chromophores. This approach offers a good balance between accuracy and efficiency, enabling comprehensive studies of TEET processes in complex environments.

# 1 Introduction

Triplet Excitation-Energy Transfer (TEET) denotes the transfer of energy from one molecule in a triplet excited state to a singlet ground-state molecule under exchange of spin states. TEET plays an important role, for example, in photosynthesis,<sup>1-3</sup> where TEET reactions prevent the generation of undesired chlorophyll triplet states in order to protect photosynthetic organisms from harmful singlet oxygen, as well as for organic photovoltaic<sup>4,5</sup> (OPV) and organic light-emitting diode<sup>6</sup> (OLED) devices. Furthermore, TEET photocatalysis<sup>7-11</sup> has gained significant importance in recent years in organic-synthetic photochemistry due to the challenges associated with directly preparing reactant molecules in triplet excited states. With respect to compounds in which direct excitation is either hampered by a very low absorption coefficient or requires very harsh short-wavelength irradiation, TEET photocatalysis provides an alternative to a direct photoexcitation approach, which allows milder and more selective access to excited states. Visible-light-mediated energy-transfer-catalysis is, for example, applied in the field of photoisomerization, enabling the expansion of cyclization reactions,<sup>12</sup> facilitating complex cascade reactions,<sup>13,14</sup> controlling systems with biological function,<sup>15</sup> and the rational design of powerful bond dissociation reactions.<sup>16</sup> Additionally, it has been employed to accelerate or enable reaction-limiting steps in transition metal catalysis.<sup>17</sup>

The concept of TEET was first introduced by Dexter in 1953 and is arguably the best-known example of Dexter Energy Transfer processes.<sup>18</sup> TEET involves the nonradiative transfer of excitation energy from an excited donor  $D^*$  to an acceptor in its ground-state  $A$



leading to the formation of the excited state of the acceptor  $A^*$ , while simultaneously regenerating the donor ground state  $D$ . TEET is often described as a simultaneous double-electron transfer between molecules without net changes in electron number or total spin states. We note, however, that more recent work has pointed out the possibility of an

alternative mechanism with step-wise electron transfer.<sup>19</sup> In a simple two-level model, TEET can be described as follows: we introduce the two diabatic states

$$\Xi_1 = |D^*(T_1)A(S_0)\rangle, \quad (2)$$

$$\Xi_2 = |A^*(T_1)D(S_0)\rangle, \quad (3)$$

whose coupling  $V$  determines the TEET rate,<sup>20</sup> with  $V$  given as

$$V = \langle \Xi_1 | \hat{H} | \Xi_2 \rangle. \quad (4)$$

Only considering the respective two frontier orbitals of both the donor and acceptor within the diabatic states, TEET would entail the transfer of one electron from the Lowest Unoccupied Molecular Orbital (LUMO) referring to the ground-state occupation of the excited triplet state of the donor  $\phi_1^D$  to the LUMO of the ground-state acceptor  $\phi_1^A$  with a simultaneous transfer of one electron with the opposite spin from the Highest Occupied Molecular Orbital (HOMO) of the acceptor  $\phi_0^A$  to the HOMO of the donor  $\phi_0^D$ . One therefore finds for the normalized wavefunctions

$$\Xi_1 = ||\phi_0^{D,\alpha} \phi_1^{D,\alpha} \phi_0^{A,\alpha} \phi_0^{A,\beta}||, \quad (5)$$

$$\Xi_2 = ||\phi_0^{D,\alpha} \phi_0^{D,\beta} \phi_0^{A,\alpha} \phi_1^{A,\alpha}||, \quad (6)$$

where  $\alpha$  and  $\beta$  denote spin functions. Inserting Eqs. (5) and (6) into Eq. (4) yields Coulomb and exchange-type contributions to the electronic coupling

$$V = \underbrace{\left( \phi_0^{D,\alpha} \phi_1^{D,\beta} | \phi_0^{A,\beta} \phi_1^{A,\alpha} \right)}_{=0} - \left( \phi_0^{D,\beta} \phi_0^{A,\beta} | \phi_1^{D,\alpha} \phi_1^{A,\alpha} \right), \quad (7)$$

where the former vanishes for TEET. We note that formally electronic couplings only arise by introducing a diabatic basis, whose choice is inherently ambiguous.

While several quantum chemical methods have been successfully applied to Singlet Excitation-Energy Transfer (SEET) calculations, TEET studies have not received as much attention. The quantum-chemical description of TEET presents a higher level of complexity compared to SEET, primarily due to the challenges associated with the short-range distance dependence of TEET and the relatively small electronic couplings involved. The complexity of TEET arises from its dependence on the spatial overlap of the orbitals and charge distributions of the different molecules, leading to an exponential decrease in the TEET rate as the distance increases. Therefore, triplet energy transfer is limited to relatively short distances. If donor and acceptor are connected via suitable bridging units, TEET may take place via superexchange as described originally by McConnell<sup>21</sup> in 1961.

Many methods developed for describing TEET couplings are based on wavefunction approaches, and are often formulated in a supersystem context. For example, Fleming and co-workers have presented two different approaches for determining TEET couplings, a direct coupling method as well as an energy-gap-based method within the Hartree–Fock (HF) theoretical framework.<sup>22</sup> In the context of one-particle and two-particle coupling interactions, Beratan and co-workers have proposed a much simpler and more intuitive approach to describe TEET couplings by predicting TEET interactions from Molecular Orbital (MO) overlaps with respect to direct and bridge-mediated donor–acceptor couplings.<sup>23</sup>

Subsystem Time-Dependent Density-Functional Theory<sup>24–27</sup> (subsystem TDDFT, sTDDFT) based on the Frozen-Density Embedding<sup>28</sup> (FDE) approach facilitates the description of excited states within a subsystem context and can be used to investigate the excited-state properties of and excitation-energy transfer couplings in complex systems, like e.g. the astaxanthin molecules in crustacyanin proteins,<sup>29</sup> the Fenna–Matthews–Olson (FMO) protein,<sup>30</sup> and porphine nanotubes.<sup>31</sup> Based on its achievements in describing SEET,<sup>32</sup> it could be assumed that subsystem TDDFT might be well-suited for TEET as well. To the best of our knowledge, this route has not been pursued so far. Therefore, the focus of this work will be on the possibility to describe TEET couplings with approximate<sup>25</sup> and “exact”<sup>27</sup> variants of

subsystem TDDFT within the coupled FDE framework. In addition, we test a mixed procedure combining subsystem TDDFT making use of Projection-based Embedding<sup>33,34</sup> (PbE) and approximate Non-Additive Kinetic Energy (NAKE) functionals in order to study TEET effects for solvated pairs of chromophores with respect to obtain a good balance between accuracy and efficiency. This method will be referred to as *mixed PbE-/NAKE-embedding* in the following.

This paper is structured as follows: First, the general theory of sTDDFT necessary to describe TEET within a subsystem context will be presented. Subsequently, the investigation of “exact” (PbE-sTDDFT) and approximate (NAKE-sTDDFT) subsystem TDDFT as well as the mixed PbE-/NAKE-embedding, will be discussed. Here, the focus is on the applicability of these methods as potential approaches for the description of TEET, starting with the analysis of several technical aspects. In the second part of this work, PbE-sTDDFT and mixed PbE-/NAKE-embedding will be applied for investigating the impact of solvent effects on TEET couplings with respect to a perylene diimide (PDI) dimer system. In addition, the effect of bridge molecules on TEET couplings in bridge-mediated donor–acceptor systems will be investigated.

## 2 Theory

### 2.1 Frozen-Density Embedding for Triplet States

Subsystem Time-Dependent Density-Functional Theory (TDDFT) is an extension of subsystem Density-Functional Theory (DFT)<sup>28,35,36</sup> for describing excited states. Starting from Frozen-Density Embedding (FDE) as a practical realization of subsystem DFT, subsystem TDDFT is based on work by Casida and Wesolowski<sup>24</sup> for embedded subsystems and was reformulated by one of us<sup>25</sup> to enable describing delocalized excitation processes in interacting chromophore aggregates.<sup>37</sup> In the unrestricted generalization of subsystem TDDFT,<sup>26</sup>

excitation energies  $\omega$  are determined as solutions of the non-Hermitian eigenvalue problem

$$\begin{pmatrix} \mathbf{A} & \mathbf{B} \\ \mathbf{B} & \mathbf{A} \end{pmatrix} \begin{pmatrix} \mathbf{X} \\ \mathbf{Y} \end{pmatrix} = \omega \begin{pmatrix} -\mathbf{1} & \mathbf{0} \\ \mathbf{0} & \mathbf{1} \end{pmatrix} \begin{pmatrix} \mathbf{X} \\ \mathbf{Y} \end{pmatrix}, \quad (8)$$

whose regular TDDFT analog is commonly referred to as Casida's equation.<sup>38</sup> In the subsystem context, the elements of the response matrices  $\mathbf{A}$  and  $\mathbf{B}$  are defined as

$$A_{(ia\sigma)_I, (jb\tau)_J} = \delta_{IJ} \delta_{ij} \delta_{ab} \delta_{\sigma\tau} (\epsilon_{a\sigma}^I - \epsilon_{i\sigma}^I) + K_{(ia\sigma)_I, (jb\tau)_J}, \quad (9)$$

$$B_{(ia\sigma)_I, (jb\tau)_J} = K_{(ia\sigma)_I, (bj\tau)_J}, \quad (10)$$

with elements of the coupling matrix  $\mathbf{K}$  (see below). Here and in the following,  $i, j$  and  $a, b$  denote occupied and virtual reference orbitals, respectively. Subscripts  $I, J$  label the subsystems involved and spin functions are denoted by  $\sigma$  and  $\tau \in \alpha, \beta$ . The eigenvectors  $(\mathbf{X} \ \mathbf{Y})^T$  gather elements of the off-diagonal blocks of the transition density matrix  $\delta D$  for each excitation

$$X_{(ia\sigma)_I} = \delta D_{(ia\sigma)_I}, \quad (11)$$

$$Y_{(ia\sigma)_I} = \delta D_{(ai\sigma)_I}. \quad (12)$$

Setting up the eigenvalue equation in Eq. (8) starting from a restricted closed-shell subsystem DFT reference leads to pairs of degenerate orbital transitions (and associated orbital-energy differences) for each spin channel and each subsystem. For the spin blocks of the coupling matrix one finds that

$$K_{\alpha\alpha} = K_{\beta\beta}, \quad (13)$$

$$K_{\alpha\beta} = K_{\beta\alpha}. \quad (14)$$

As a result, the eigenvalue problem in Eq. (8) decouples into two separate eigenvalue equations of identical structure with symmetric (+) and antisymmetric (−) combinations of the coupling matrix

$$K^{(\pm)} = K_{\alpha\alpha}^{(\pm)} \pm K_{\alpha\beta}^{(\pm)}. \quad (15)$$

The singlet and triplet eigenvalue problems can therefore be derived as simple unitary transformations of the unrestricted response problem with eigenstates

$$\delta D_{(pq)_I}^{(\pm)} = \frac{1}{\sqrt{2}} (\delta D_{(pq\alpha)_I} \pm \delta D_{(pq\beta)_I}), \quad pq \in ia, ai, \quad (16)$$

directly enabling to discriminate between singlet (which are spin-symmetry-conserving and correspond to the (+) combination) and triplet excitations (which are spin-symmetry breaking and correspond to the (−) combination).<sup>39</sup>

While the orbital-energy differences on the diagonal of the  $\mathbf{A}$  matrix are retained for both the singlet and triplet eigenvalue equation, the coupling matrix requires further consideration. We refer the reader to Refs. 40 and 41 for a more detailed discussion of the singlet coupling matrix of subsystem TDDFT. Using Mulliken’s notation for two-electron integrals, elements of the triplet coupling matrix  $\mathbf{K}^{(-)}$  can be written as

$$\begin{aligned} K_{(ia)_I, (jb)_J}^{(-)} = & \delta_{IJ} [(\phi_i^I \phi_a^I | f_{xc}^{I, \alpha\alpha} - f_{xc}^{I, \alpha\beta} | \phi_j^J \phi_b^J) - c_{\text{HF}}^I (\phi_i^I \phi_j^J | \phi_a^I \phi_b^J)] \\ & + (\phi_i^I \phi_a^I | f_{xc}^{\text{nadd}, \alpha\alpha} - f_{xc}^{\text{nadd}, \alpha\beta} | \phi_j^J \phi_b^J) + (\phi_i^I \phi_a^I | f_{\text{kin}}^{\text{nadd}, \alpha\alpha} - f_{\text{kin}}^{\text{nadd}, \alpha\beta} | \phi_j^J \phi_b^J), \end{aligned} \quad (17)$$

with the exchange–correlation (XC) energy kernel of subsystem  $I$

$$f_{xc}^{I, \sigma\tau}(\mathbf{r}, \mathbf{r}') = \left. \frac{\delta^2 E_{xc}[\rho]}{\delta \rho^\sigma(\mathbf{r}) \delta \rho^\tau(\mathbf{r}')} \right|_{\rho=\rho_I}, \quad (18)$$

where  $c_{\text{HF}}^I$  is the amount of Hartree–Fock exchange in the functional approximation used for



evaluating  $f_{xc}^I$ . Likewise, one finds for the non-additive kinetic and XC energy kernels,  $f_{kin}^{nadd}$  and  $f_{xc}^{nadd}$  with energy functionals  $F = T_s, E_{xc}$ , that

$$f^{nadd,\sigma\tau}(\mathbf{r}, \mathbf{r}') = \left. \frac{\delta^2 F[\rho]}{\delta\rho^\sigma(\mathbf{r})\delta\rho^\tau(\mathbf{r}')} \right|_{\rho=\rho_{tot}} - \delta_{IJ} \left. \frac{\delta^2 F[\rho]}{\delta\rho^\sigma(\mathbf{r})\delta\rho^\tau(\mathbf{r}')} \right|_{\rho=\rho_I}. \quad (19)$$

Following the adiabatic approximation, the subsystem densities  $\rho_I$  and the supersystem density  $\rho_{tot}$  are evaluated with the corresponding electronic ground-state solutions. For the sake of completeness, the full triplet subsystem TDDFT eigenvalue equation therefore reads

$$\begin{pmatrix} \bar{\mathbf{A}} & \bar{\mathbf{B}} \\ \bar{\mathbf{B}} & \bar{\mathbf{A}} \end{pmatrix} \begin{pmatrix} \bar{\mathbf{X}} \\ \bar{\mathbf{Y}} \end{pmatrix} = \bar{\omega} \begin{pmatrix} -1 & \mathbf{0} \\ \mathbf{0} & 1 \end{pmatrix} \begin{pmatrix} \bar{\mathbf{X}} \\ \bar{\mathbf{Y}} \end{pmatrix}, \quad (20)$$

with

$$\bar{A}_{(ia)_I,(jb)_J} = \delta_{IJ}\delta_{ij}\delta_{ab}(\epsilon_a^I - \epsilon_i^I) + K_{(ia)_I,(jb)_J}^{(-)}, \quad (21)$$

$$\bar{B}_{(ia)_I,(jb)_J} = K_{(ia)_I,(bj)_J}^{(-)}. \quad (22)$$

The key differences to the singlet eigenvalue problem are (i) the Coulomb coupling matrix elements vanish and (ii) different functional derivatives need to be evaluated for each component of the kernel. The main challenge for the extension of an existing singlet or unrestricted subsystem TDDFT code for computing triplet excitations from restricted references is to evaluate the appropriate functional derivatives for the numerical integration of the XC as well as non-additive XC and kinetic kernels. For a discussion of the corresponding terms in regular TDDFT, see Ref. 39. On the contrary, however, Hartree–Fock exchange contributions to the triplet coupling matrix are the same as in the singlet case. Further, due to the conserved structure of the eigenvalue problem, identical (iterative) solution strategies as used for Eq. (8) can be applied for Eq. (20). This work focuses on the Tamm–Dancoff Approximation (TDA)<sup>42</sup> of subsystem TDDFT.<sup>37</sup> Neglecting the  $\mathbf{B}$  matrix in the eigenvalue problem, the subsystem

TDDFT eigenvalue problem turns into a Hermitian eigenvalue problem of reduced dimension

$$\bar{\mathbf{A}}\bar{\mathbf{X}} = \bar{\omega}\bar{\mathbf{X}}, \quad (23)$$

allowing for a more straightforward diagonalization process. Another important implication of the TDA in the subsystem TDDFT context is that electronic couplings can be calculated directly,<sup>37</sup> as outlined below.

Subsystem TDDFT in practice is typically performed in a two-step procedure as first outlined in Ref. 25. In the first step, referred to as uncoupled Frozen-Density Embedding (FDEu), some of the lowest-lying excitations of each subsystem are determined separately. This is done by (partially) diagonalizing the intra-subsystem blocks of the response matrices appearing in Eqs. (8) or (20), yielding a set of FDEu excitation energies and transition densities. In the subsequent step, known as coupled Frozen-Density Embedding (FDEc), the obtained FDEu transition densities are first used to construct a transformation matrix  $\mathbf{U}$ , which is then employed to transform the full subsystem (TDA-)TDDFT response problem into the subspace spanned by the FDEu excitation vectors

$$\mathbf{U}^T \bar{\mathbf{A}} \mathbf{U} \mathbf{U}^T \bar{\mathbf{X}} = \omega^{\text{FDEc}} \mathbf{U}^T \bar{\mathbf{X}}, \quad (24)$$

$$\tilde{\mathbf{A}} \tilde{\mathbf{X}} = \omega^{\text{FDEc}} \tilde{\mathbf{X}}, \quad (25)$$

introducing the FDEc subspace matrix  $\tilde{\mathbf{A}}$  with elements

$$\tilde{A}_{(m)_I(n)_J} = \sum_{(ia)_I} \sum_{(jb)_J} \bar{X}_{(ia)_I}^m \bar{A}_{(ia)_I, (jb)_J} \bar{X}_{(jb)_J}^n, \quad (26)$$

where subscripts  $(m)_I$  and  $(n)_J$  denote FDEu excitations  $m$  and  $n$  of subsystem  $I$  and  $J$ , respectively. The block structure of the subsystem TDA-TDDFT eigenvalue problem implies

that Eq. (26) can be conveniently rewritten as

$$\tilde{\tilde{A}}_{(m)I(n)J} = \delta_{IJ}\delta_{mn}\omega_m^I + (1 - \delta_{IJ})V_{(m)I(n)J}, \quad (27)$$

such that off-diagonal blocks contain the electronic couplings  $V_{(m)I(n)J}$  and the diagonal comprises the uncoupled excitation energies  $\omega_m^I$ . Following an exciton picture, the  $\tilde{\tilde{A}}$  matrix can thus be interpreted as a triplet Hamilton-like matrix. To avoid any ambiguity, we semantically distinguish between (i) the electronic couplings  $V$  extracted from the off-diagonal blocks of the FDEc subspace matrix (which are interpreted as Triplet Excitation-Energy Transfer (TEET) couplings in this work) and (ii) elements of the triplet coupling matrix  $\mathbf{K}^{(-)}$ .

## 2.2 Projection-based Embedding

Similar to FDE in the original sense,<sup>28,35</sup> projection-based embedding (PbE) partitions the supersystem density into subsystem densities. To avoid issues associated with the non-additivity of the subsystem kinetic energies in FDE, projection-based embedding enforces inter-subsystem or external-orthogonality (EO) of the subsystem orbitals by virtue of a non-local projector  $\hat{P}_B$ ,

$$\hat{P}_B = \sum_j^{n_B} |\phi_j^B\rangle \langle \phi_j^B|, \quad (28)$$

for a system consisting of an active system  $A$  embedded in an environmental subsystem  $B$  with  $n_B$  occupied environment orbitals  $\phi_j^B$ . Projection-based embedding in practice involves adding a particular projection operator  $\hat{O}$  to the supersystem Fock operator  $\hat{F}$  to obtain the active subsystem's orbitals  $\phi_i^A$ ,

$$(\hat{F} + \hat{O}) |\phi_i^A\rangle = \epsilon_i^A |\phi_i^A\rangle. \quad (29)$$

Several projection operators have been presented in the literature. This work focuses on the levelshift operator<sup>33</sup>

$$\hat{O}^{\text{level.}} = \lim_{\mu \rightarrow \infty} \mu \hat{P}_B, \quad (30)$$

with a levelshift parameter  $\mu$ , as well as on the Huzinaga operator<sup>43</sup>

$$\hat{O}^{\text{Huz.}} = -[\hat{F}, \hat{P}^B]_+. \quad (31)$$

The usage of projection operators formally replaces NAKE kernel contributions of the coupling matrix  $\mathbf{K}$  with density matrix ( $\mathbf{D}$ ) derivatives of the EO potential in matrix representation  $\mathbf{V}^{\text{EO}}$ . These were originally derived in Ref. 44 for the levelshift operator as well as corrected and further discussed in Refs. 27 and 40. We find for EO kernel contributions of the levelshift operator to the triplet coupling matrix,

$$K_{(ia)_I, (jb)_J}^{(-), \text{EO}, \text{level.}} = \frac{\partial V_{(ia)_I}^{\text{EO}, \text{level.}}}{\partial D_{(jb\alpha)_J}} - \frac{\partial V_{(ia\alpha)_I}^{\text{EO}, \text{level.}}}{\partial D_{(jb\beta)_J}} \quad (32)$$

$$= \mu \langle \phi_{i\alpha}^I | \phi_{j\alpha}^J \rangle \langle \phi_{b\alpha}^J | \phi_{a\alpha}^I \rangle - \mu \langle \phi_{i\alpha}^I | \phi_{j\beta}^J \rangle \langle \phi_{b\beta}^J | \phi_{a\alpha}^I \rangle \quad (33)$$

$$= \mu \langle \phi_i^I | \phi_j^J \rangle \langle \phi_b^J | \phi_a^I \rangle, \quad (34)$$

where the second summand trivially vanishes due to spin-function orthogonality rendering the resulting expression identical to the singlet case. Similar arguments can be given for the Huzinaga EO kernel,<sup>40</sup>

$$K_{(ia)_I, (jb)_J}^{(-), \text{EO}, \text{Huz.}} = \frac{\partial V_{(ia\alpha)_I}^{\text{EO}, \text{Huz.}}}{\partial D_{(jb\alpha)_J}} - \frac{\partial V_{(ia\alpha)_I}^{\text{EO}, \text{Huz.}}}{\partial D_{(jb\beta)_J}} \quad (35)$$

$$= -\langle \phi_i^I | \hat{F} | \phi_j^J \rangle \langle \phi_b^J | \phi_a^I \rangle. \quad (36)$$

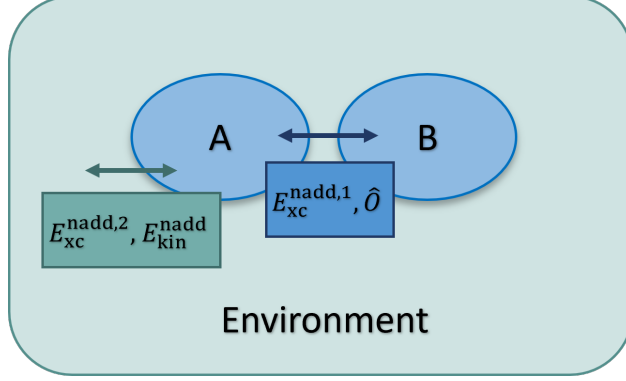


Figure 1: Illustration of mixed PbE-/NAKE-embedding with subsystem  $A$  and  $B$  being described using PbE-sTDDFT with inter-subsystem exchange–correlation functional  $E_{xc}^{nadd,1}$  and projection operator  $\hat{O}$  and the environment using NAKE-sTDDFT with  $E_{xc}^{nadd,2}$  and non-additive kinetic energy functional  $E_{kin}^{nadd}$ .

Collecting terms, elements of the triplet coupling matrix in subsystem TDDFT with projection-based embedding read

$$K_{(ia)_I,(jb)_J}^{(-)} = \delta_{IJ} \left[ (\phi_i^I \phi_a^I | f_{xc}^{I,\alpha\alpha} - f_{xc}^{I,\alpha\beta} | \phi_j^J \phi_b^J) - c_{HF}^I (\phi_i^I \phi_j^J | \phi_a^I \phi_b^J) + c_{HF}^{nadd} (\phi_i^I \phi_j^J | \phi_a^I \phi_b^J) \right] \\ + (\phi_i^I \phi_a^I | f_{xc}^{nadd,\alpha\alpha} - f_{xc}^{nadd,\alpha\beta} | \phi_j^J \phi_b^J) - c_{HF}^{nadd} (\phi_i^I \phi_j^J | \phi_a^I \phi_b^J) + K_{(ia)_I,(jb)_J}^{(-),EO}, \quad (37)$$

where inter-subsystem orbital orthogonality allows for inter-subsystem Hartree–Fock exchange via the functional approximation used for evaluating the non-additive XC kernel (which can, in principle, be chosen independently of the intra-subsystem XC approximation). The corresponding amount is labeled  $c_{HF}^{nadd}$ .

This work further employs the Fermi-shifted Huzinaga potential,<sup>45</sup> for which, to the best of our knowledge, no EO kernel has been presented in the literature yet. A brief derivation is given in the appendix of this article.

### 2.3 Mixed PbE-/NAKE-Embedding

In order to enable a more efficient description of complex systems, we introduce a combined embedding approach for investigating environmental effects on sub-parts of the considered

system. The idea of this *mixed PbE-/NAKE-embedding*<sup>46</sup> procedure, schematically depicted in Fig. 1, is the partitioning of the electronic density into two subspaces belonging to  $N_{\text{PbE}}$  subsystems described using PbE-sTDDFT with density  $\rho_{\text{PbE}}$  (exact embedding), and  $N_{\text{NAKE}}$  subsystems described by NAKE-sTDDFT with density  $\rho_{\text{NAKE}}$  (approximate embedding),

$$\rho_{\text{tot}}(\mathbf{r}) = \rho_{\text{PbE}}(\mathbf{r}) + \rho_{\text{NAKE}}(\mathbf{r}) \quad (38)$$

$$= \sum_I^{N_{\text{PbE}}} \rho_I(\mathbf{r}) + \sum_J^{N_{\text{NAKE}}} \rho_J(\mathbf{r}). \quad (39)$$

This partitioning is illustrated in Fig. 1, where  $\rho_{\text{PbE}}$  corresponds to the density of the subsystems A and B, while  $\rho_{\text{NAKE}}$  corresponds to the environment density. Within each subspace, the densities are obtained from an arbitrary number of assigned subsystems. The system's total energy is expressed as a combination of Kohn–Sham energies, interaction energies, and two different non-additive exchange–correlation contributions

$$\begin{aligned} E &= \sum_I^{N_{\text{PbE}}} E^{\text{KS}}[\rho_I] + \sum_J^{N_{\text{NAKE}}} E^{\text{KS}}[\rho_J] + J[\{\rho_K\}] + V_{\text{nuc,el}}[\{\rho_K\}] \\ &+ E_{\text{xc}}^{\text{nadd},1}[\rho_{\text{PbE}}, \{\rho_I\}] + E_{\text{xc}}^{\text{nadd},2}[\rho_{\text{tot}}, \rho_{\text{PbE}}, \{\rho_J\}] \\ &+ T_s^{\text{nadd}}[\rho_{\text{tot}}, \rho_{\text{PbE}}, \{\rho_J\}], \end{aligned} \quad (40)$$

one associated with the PbE region  $E_{\text{xc}}^{\text{nadd},1}$  and the other with the remaining part of the system  $E_{\text{xc}}^{\text{nadd},2}$ . For the non-additive part associated with the PbE region, the non-additive exchange–correlation contribution is given by

$$E_{\text{xc}}^{\text{nadd},1}[\rho_{\text{PbE}}, \{\rho_I\}] = E_{\text{xc}}[\rho_{\text{PbE}}] - \sum_I^{N_{\text{PbE}}} E_{\text{xc}}[\rho_I], \quad (41)$$

and for the remaining part of the system, the non-additive XC functional contribution can be determined as

$$E_{\text{xc}}^{\text{nadd},2}[\rho_{\text{tot}}, \rho_{\text{PbE}}, \{\rho_J\}] = E_{\text{xc}}[\rho_{\text{tot}}] - \sum_J^{N_{\text{NAKE}}} E_{\text{xc}}[\rho_J] - E_{\text{xc}}[\rho_{\text{PbE}}]. \quad (42)$$

Note that in principle different approximate XC functionals can be used for the evaluation of these contributions. The non-additive kinetic energy is calculated similarly,

$$T_s^{\text{nadd}}[\rho_{\text{tot}}, \rho_{\text{PbE}}, \{\rho_J\}] = T_s[\rho_{\text{tot}}] - \sum_J^{N_{\text{NAKE}}} T_s[\rho_J] - T_s[\rho_{\text{PbE}}]. \quad (43)$$

The Kohn–Sham equations with constrained electron density (KSCED) within the mixed PbE-/NAKE-embedding approach are given as

$$\left( -\frac{\nabla^2}{2} + \hat{v}_{\text{eff}}^K + \hat{v}_{\text{emb}}^K \right) \phi_i^K = \epsilon_i^K \phi_i^K, \quad (44)$$

where  $\hat{v}_{\text{eff}}^K$  is the Kohn–Sham effective potential evaluated for subsystem  $K$ . The embedding potential  $\hat{v}_{\text{emb}}^K$  for a subsystem  $K$  in the NAKE region can be expressed as

$$\begin{aligned} \hat{v}_{\text{emb}}^K[\rho_K, \rho_{\text{PbE}}, \rho_{\text{tot}}](\mathbf{r}) = & \sum_{L \neq K}^{N_{\text{NAKE}} + N_{\text{PbE}}} \left[ \int \frac{\rho_L(\mathbf{r}')}{|\mathbf{r}' - \mathbf{r}|} d\mathbf{r}' - \sum_{\alpha \in L} \frac{Z_\alpha}{|\mathbf{r} - \mathbf{R}_\alpha|} \right] \\ & + \frac{\delta E_{\text{xc}}[\rho_{\text{tot}}]}{\delta \rho_{\text{tot}}(\mathbf{r})} - \frac{\delta E_{\text{xc}}[\rho_K]}{\delta \rho_K(\mathbf{r})} \\ & + \frac{\delta T_s[\rho_{\text{tot}}]}{\delta \rho_{\text{tot}}(\mathbf{r})} - \frac{\delta T_s[\rho_K]}{\delta \rho_K(\mathbf{r})}. \end{aligned} \quad (45)$$

For a subsystem  $K$  in the PbE region,  $\hat{v}_{\text{emb}}^K$  becomes a non-local operator through the projection operator  $\hat{O}$  [see Eqs. (30) and (31)] and reads

$$\begin{aligned} \hat{v}_{\text{emb}}^K = & \sum_{L \neq K}^{N_{\text{NAKE}} + N_{\text{PbE}}} \left[ \int \frac{\rho_L(\mathbf{r}')}{|\mathbf{r} - \mathbf{r}'|} d\mathbf{r}' - \sum_{\alpha \in L} \frac{Z_\alpha}{|\mathbf{r} - \mathbf{R}_\alpha|} \right] \\ & + \frac{\delta E_{\text{xc}}[\rho_{\text{tot}}]}{\delta \rho_{\text{tot}}(\mathbf{r})} - \frac{\delta E_{\text{xc}}[\rho_{\text{PbE}}]}{\delta \rho_{\text{PbE}}(\mathbf{r})} + \frac{\delta \tilde{E}_{\text{xc}}[\rho_{\text{PbE}}]}{\delta \rho_{\text{PbE}}(\mathbf{r})} - \frac{\delta \tilde{E}_{\text{xc}}[\rho_K]}{\delta \rho_K(\mathbf{r})} \\ & + \frac{\delta T_s[\rho_{\text{tot}}]}{\delta \rho_{\text{tot}}(\mathbf{r})} - \frac{\delta T_s[\rho_{\text{PbE}}]}{\delta \rho_{\text{PbE}}(\mathbf{r})} + \hat{O}, \end{aligned} \quad (46)$$

where the tilde refers to the XC potential contributions arising from the non-additive XC energy associated with the PbE region.

In the sTDDFT context, the mixed PbE-/NAKE-embedding coupling matrix is likewise obtained from derivatives of matrix elements of the electronic potential of subsystem  $I$

$$\hat{v}_{\text{el}}^I = \hat{v}_{\text{eff}}^I + \hat{v}_{\text{emb}}^I \quad (47)$$

with respect to elements of the density matrix  $\mathbf{D}$  of subsystem  $K$

$$K_{(ia)_I, (jb)_K} = \frac{\partial v_{\text{el}, (ia)}^I}{\partial D_{(jb)_K}}, \quad (48)$$

and is defined as (in the non-spin-resolved case)

$$\begin{aligned} K_{(ia)_I, (jb)_K} = & \left( \phi_a^I \phi_b^I | \phi_j^K \phi_b^K \right) + \left( \phi_a^I \phi_b^I \left| f_{\text{xc}}^{\text{tot}} + f_{\text{kin}}^{\text{tot}} - f_{\text{xc}}^{\text{PbE}} - f_{\text{kin}}^{\text{PbE}} + \tilde{f}_{\text{xc}}^{\text{PbE}} \right| \phi_j^K \phi_b^K \right) \\ & + \delta_{IK} \left[ \left( \phi_a^I \phi_b^I \left| f_{\text{xc}}^{\text{intra}, I} - \tilde{f}_{\text{xc}}^{\text{PbE}, I} \right| \phi_j^K \phi_b^K \right) \right] + K_{(ia)_I, (jb)_K}^{\text{EO}} \end{aligned} \quad (49)$$

for  $I$  and  $K$  being both part of the PbE region. With  $F = T_s, E_{\text{xc}}$ , the various kinetic and



exchange–correlation kernel contributions in Eq. (49) follow the definitions

$$f^{\text{tot}}(\mathbf{r}, \mathbf{r}') = \left. \frac{\delta^2 F[\rho]}{\delta\rho(\mathbf{r})\delta\rho(\mathbf{r}')} \right|_{\rho=\rho_{\text{tot}}}, \quad (50)$$

$$f^{\text{PbE}}(\mathbf{r}, \mathbf{r}') = \left. \frac{\delta^2 F[\rho]}{\delta\rho(\mathbf{r})\delta\rho(\mathbf{r}')} \right|_{\rho=\rho_{\text{PbE}}}, \quad (51)$$

$$\tilde{f}_{\text{xc}}^{\text{PbE}}(\mathbf{r}, \mathbf{r}') = \left. \frac{\delta^2 \tilde{E}_{\text{xc}}[\rho]}{\delta\rho(\mathbf{r})\delta\rho(\mathbf{r}')} \right|_{\rho=\rho_{\text{PbE}}}, \quad (52)$$

$$f_{\text{xc}}^{\text{intra},I}(\mathbf{r}, \mathbf{r}') = \left. \frac{\delta^2 E_{\text{xc}}[\rho]}{\delta\rho(\mathbf{r})\delta\rho(\mathbf{r}')} \right|_{\rho=\rho_I}, \quad (53)$$

$$\tilde{f}_{\text{xc}}^{\text{PbE},I}(\mathbf{r}, \mathbf{r}') = \left. \frac{\delta^2 \tilde{E}_{\text{xc}}[\rho]}{\delta\rho(\mathbf{r})\delta\rho(\mathbf{r}')} \right|_{\rho=\rho_I}. \quad (54)$$

In the case of  $I$  being part of the PbE region and  $K$  of the NAKE region, the kernel is given as

$$K_{(ia)_I,(jb)_K} = (\phi_i^I \phi_a^I | \phi_j^K \phi_b^K) + (\phi_i^I \phi_a^I | f_{\text{xc}}^{\text{tot}} + f_{\text{kin}}^{\text{tot}} | \phi_j^K \phi_b^K), \quad (55)$$

and for  $I$  and  $K$  being both part of the NAKE region, it can be expressed as

$$K_{(ia)_I,(jb)_K} = (\phi_i^I \phi_a^I | \phi_j^K \phi_b^K) + (\phi_i^I \phi_a^I | f_{\text{xc}}^{\text{nadd}} + f_{\text{kin}}^{\text{nadd}} | \phi_j^K \phi_b^K) + \delta_{IK} (\phi_i^I \phi_a^I | f_{\text{xc}}^{\text{intra},I} | \phi_j^K \phi_b^K), \quad (56)$$

where the non-additive contributions follow directly from Eq. (19) (without the explicit inclusion of HF exchange in any exchange–correlation functional approximation for brevity). Note that Eq. (55) only becomes relevant for FDEc-TDDFT calculations, while Eqs. (49) and (56) may also be needed in FDEu-TDDFT calculations for the case of identical subsystem labels  $I, K$ . This allows to describe the subspace of interest using “exact” PbE embedding while describing the remaining subsystems associated to the environment with approximate embedding. Therefore, environmental effects like the effect of an explicit solvent on electronic couplings can be studied more efficiently without compromising accuracy for the coupled chromophores.

For mixed PbE-/NAKE-embedding, the following notation will be used in this article:

Intra-XC/[Inter1-XC, Inter2-XC]/[ $\hat{O}$ , NAKE func.]. Here, Intra-XC refers to the XC functional for intra-subsystem interactions, Inter1-XC denotes the inter-subsystem XC functional of the two active subsystems and Inter2-XC is used for the remaining inter-subsystem interactions. Additionally, the projection operator  $\hat{O}$  for the exact embedding approach is given as well as the NAKE functional, denoted as NAKE func., used in the approximate embedding approach.

### 3 Computational Details

All technical test calculations in the following were performed using the helium dimer and fluoroethylene dimer as test systems. The geometry of the latter was optimized with TURBOMOLE 7.5.1<sup>47</sup> using PBE0<sup>48</sup> as the exchange–correlation functional and a def2-TZVP<sup>49</sup> basis set. The structures of the perylene diimide (PDI) dimer in water were taken from Ref. 50, while those for the PDI dimer in other solvents were obtained from Ref. 51. All calculations were performed with a slightly modified version of the SERENITY program (1.5.2).<sup>52–54</sup> Unless stated otherwise, all supersystem and subsystem TDDFT calculations were performed with this version of SERENITY using the PBE0 XC functional and the def2-SVP<sup>49</sup> basis set. All self-consistent field (SCF) procedures were stopped as soon as two of the following convergence criteria were fulfilled: total energy threshold of  $5 \cdot 10^{-8} E_h$ , root-mean-square deviation of the density matrix threshold of  $1 \cdot 10^{-8}$  a.u., as well as a threshold of  $5 \cdot 10^{-7}$  a.u. for the commutator of the Fock and density matrix. The intrinsic-bond orbital localization method<sup>55</sup> is used in projection-based embedding calculations. Moreover, the Tamm–Dancoff approximation (TDA) was used in each calculation and the six lowest-lying excitation energies for each subsystem and the twelve lowest-lying excitation energies for each supersystem were determined. The eigenvectors of the iterative solution procedure of the TDA problem were converged to maximum residual norms of  $10^{-5}$ . Additionally, for embedding calculations, PW91<sup>56</sup> was used as the non-additive XC functional and PW91k<sup>57</sup> as the non-additive kinetic-energy functional in the case of NAKE-sTDDFT calculations. In case of

PbE-sTDDFT, PBE0 was chosen as the non-additive XC functional in combination with the levelshift projection operator if not mentioned otherwise. All mixed PbE-/NAKE-embedding calculations were performed using the following settings: [PBE0, PBE]/[PBE0, PBE]/[level., PW91K], def2-SVP. Note that, unless stated otherwise, the obtained results were determined for excitations dominated by  $\text{HOMO}(\pi) \rightarrow \text{LUMO}(\pi^*)$  transitions and their corresponding electronic couplings.

## 4 Results and Discussion

### 4.1 Subsystem TDDFT for TEET Couplings

#### 4.1.1 Helium Dimer

In the following, we will investigate the applicability of (subsystem) TDDFT for the description of triplet excitation-energy transfer processes based on the helium dimer as an initial model system. Therefore, we present a comparison of the TEET and SEET descriptions using (i) approximate embedding (NAKE-sTDDFT), as well as (ii) “exact” embedding (PbE-sTDDFT). Note that the NAKE-sTDDFT as well as the isolated calculations were performed using a supersystem basis. For the sake of completeness, it is important to mention that the excitation energies related to charge-transfer transitions of the analyzed excitation, stemming from the utilization of the supersystem basis, are also present in the results (as depicted in Fig. 2). However, it is worth emphasizing that these excitation energies lack physical significance in the context of isolated and FDEu calculations<sup>58</sup> and therefore, will not be further discussed.

Fig. 2a shows the excitation energies of the  $\text{HOMO} \rightarrow \text{LUMO}$  triplet (green lines) local excitation (LE) for an inter-subsystem separation of 1.0 Å obtained with PbE-sTDDFT using the Fermi-shifted Huzinaga operator (see Appendix). Moreover, the figure also illustrates the electronic couplings  $V$  associated with this transition, which are directly related to the TEET

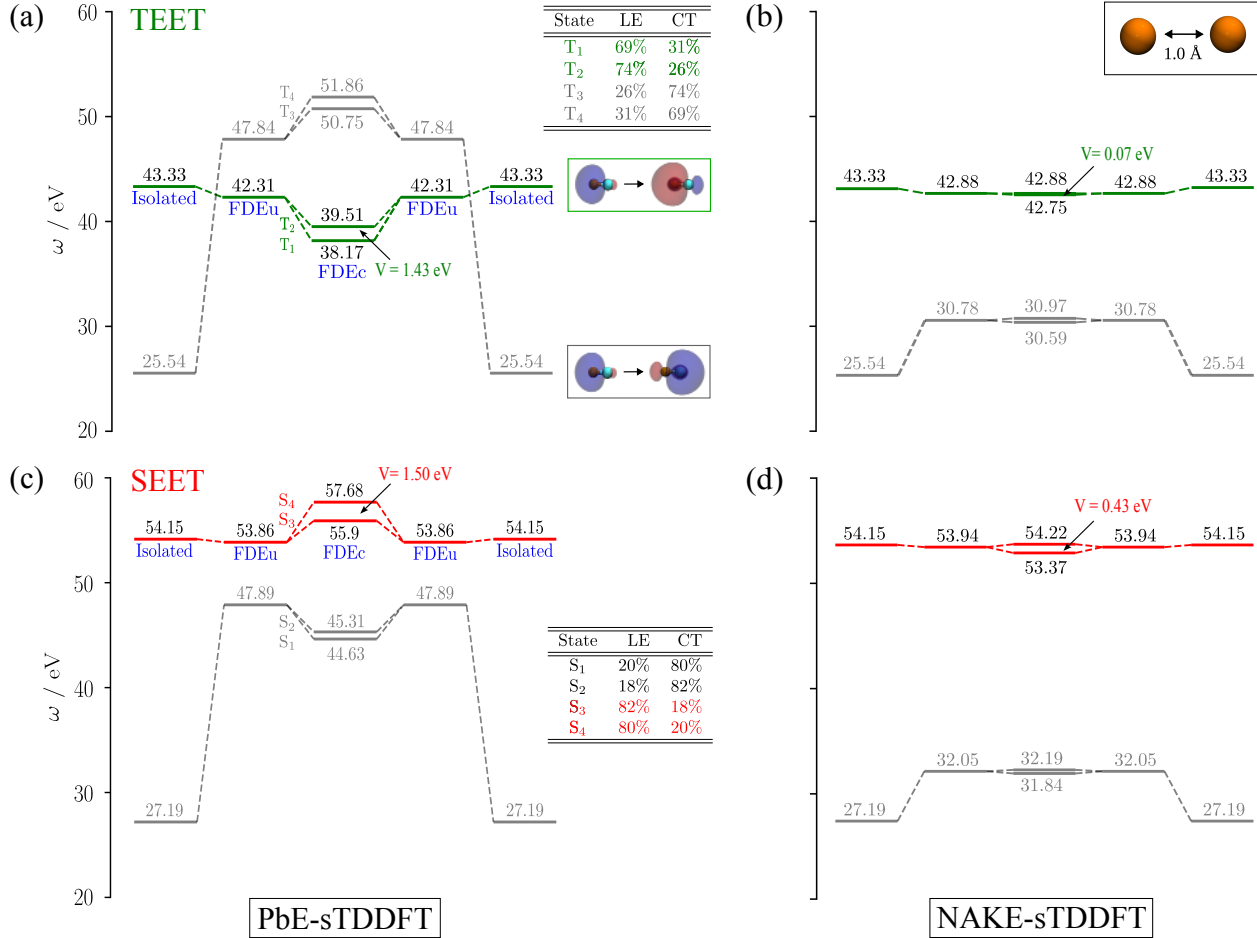


Figure 2: Excitation energies  $\omega$  and electronic couplings  $V$  (in eV), represented by colored values, of the triplet (green) and singlet (red) HOMO  $\rightarrow$  LUMO local excitation (LE) of the helium dimer at 1.0 Å separation calculated using TDDFT [PBE0, 6-31G] for isolated systems, as well as uncoupled (FDEu), and coupled (FDEc). (a) and (c), PbE-sTDDFT [PbE: PBE0/PBE0/Fermi-shifted Huzinaga, 6-31G]; (b) and (d), NAKE-sTDDFT [NAKE: PBE0/PW91/PW91K, 6-31G]. Gray lines correspond to the triplet HOMO  $\rightarrow$  LUMO charge-transfer (CT) excitations and to the corresponding singlet CT transitions. A supermolecular basis was used in all cases.

coupling in a simple effective exciton model. We have numerically verified that the triplet excitation energies of the helium dimer as obtained from supermolecular TDDFT calculations are reproduced using coupled PbE-sTDDFT. As a result, we omit the supersystem results for simplicity.

First, Fig. 2a illustrates a comparison of TEET excitation energies obtained from different approaches: isolated TDDFT, FDEu-, and FDEc-TDDFT, revealing the impact of the

embedding potential on the excitation energies. To analyze TEET effects, we first have to identify the corresponding triplet excitations. While this is straightforward for the isolated system, already the FDEu results show triplet excitations of mixed local excitation and charge-transfer character. For instance, the FDEu-PbE triplet excitation at 42.31 eV shows 62% LE and 38% CT character. The dominant orbital transitions of the triplet excitations are shown in Tab. S1 in the Supporting Information (SI), including the distinction between LE and CT transitions. Here, we decomposed the response of the system into local and CT contributions using the virtual-orbital-space localization method.<sup>59</sup> The FDEu-TDDFT vertical excitation energies show a noticeable decrease compared to the isolated case (43.33 eV), whereas the inclusion of inter-subsystem coupling effects leads to a splitting of FDEu energies into FDEc-TDDFT excitation energies at 38.17 and 39.51 eV. These findings highlight the importance of the embedding approach in accurately describing excitation energies and demonstrates the importance of considering environmental effects and inter-subsystem interactions.

In the case of NAKE-sTDDFT, we investigate the excitation corresponding to the HOMO  $\rightarrow$  LUMO LE transition considered in the PbE-sTDDFT calculations (see Fig. 2b). The excitation energy decreases from 43.33 eV (isolated atom) to 42.88 eV when considering the active subsystem in the presence of the environmental subsystem. The splitting of the FDEu excitation energy into FDEc energies is significantly larger in PbE-sTDDFT compared to NAKE-sTDDFT. Apart from the obvious difference in the treatment of the non-additive kinetic energy and external-orthogonality, also the mixing with charge-transfer excitations in the PbE case may lead to differences in the resulting energy splittings (see Tab. S1 in the SI). Furthermore, the triplet excitation remains similarly stabilized in both NAKE- and PbE-sTDDFT methods, exhibiting minimal variation in energy between the two approaches. With respect to the electronic coupling, the TEET coupling obtained from NAKE-sTDDFT (0.07 eV) differs from that of the PbE-sTDDFT calculation (1.43 eV) by about a factor of 20. This indicates that NAKE-sTDDFT significantly underestimates TEET electronic couplings, rendering it inadequate for accurately describing TEET couplings dominated by short-range

effects.

Fig. 2c shows the corresponding singlet (red lines) HOMO  $\rightarrow$  LUMO LE transition of the helium dimer test system. Additionally to the triplet excitation, the dominant orbital transitions of the singlet excitations are shown in Tab. S2 in the SI. For SEET, energies of 54.15 eV in the isolated case and 53.86 eV in the FDEu case are obtained with PbE which splits to 55.90 and 57.68 eV in the coupled FDE step. In the PbE case, the considered singlet transition shows approximately 80% LE and 20% CT character and a SEET coupling of 1.50 eV.

When comparing the isolated and FDEu results, it is evident that the reduction in energy for the singlet excitation is quite similar when using the PbE and NAKE (53.94 eV) versions (see Fig. 2d). In both cases, the singlet excitation energy is decreased by approximately 0.2 to 0.3 eV. Moreover, we observe that the SEET electronic coupling of the singlet HOMO  $\rightarrow$  LUMO LE transition shows slightly lower values for NAKE- (0.43 eV) than for PbE-sTDDFT (1.50 eV). This indicates that both embedding methods provide a description of approximately equal quality of the SEET coupling for this specific transition, consistent with findings from other studies on SEET couplings.<sup>32</sup> It is important to mention that we do not achieve identical results due to the approximations employed in the NAKE-sTDDFT method.

When comparing the electronic coupling of triplet and singlet excitations, the situation is different for SEET couplings: Even though NAKE-sTDDFT yields a value considerably lower than PbE-sTDDFT, the difference is not an order of magnitude and can at least partially be explained by the use of different inter-subsystem XC functionals, an aspect that will be further analyzed below.

#### **4.1.2 Fluoroethylene Dimer: Dependence on the Intra- and Inter-XC Approximations**

As another example we analyze the HOMO( $\pi$ )  $\rightarrow$  LUMO( $\pi^*$ ) triplet excitation of a fluoroethylene dimer as a function of the inter-subsystem separation. In this context, we investigate

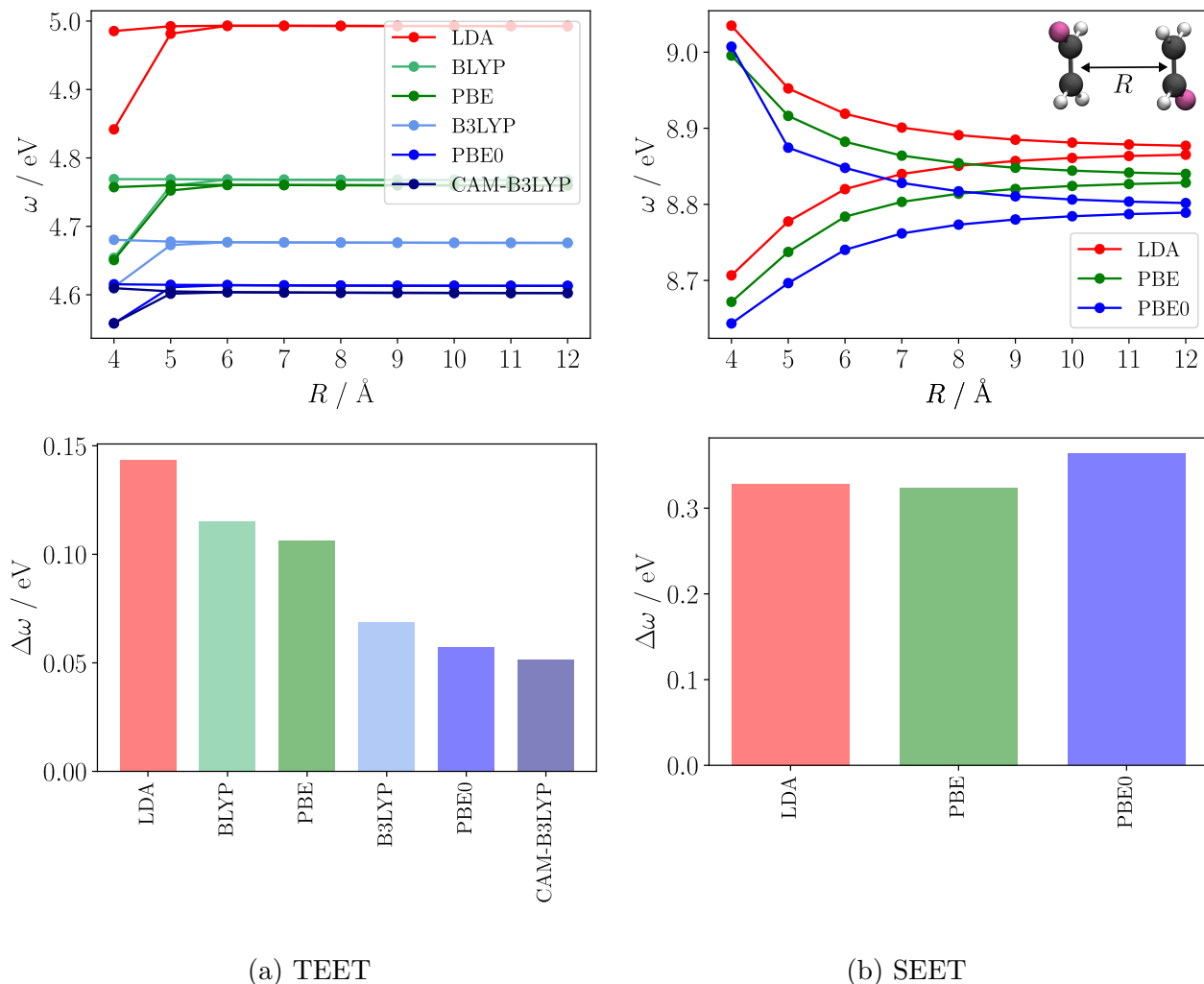


Figure 3: Excitation energies  $\omega$  (top) of the  $\pi \rightarrow \pi^*$  (a) triplet and (b) singlet excitation as a function of the inter-subsystem separation and splittings  $\Delta\omega$  (bottom) for an inter-subsystem separation of  $R = 4.0 \text{ \AA}$  of the fluoroethylene dimer obtained from supersystem calculations regarding the exchange–correlation functional dependence [Supersystem: (LDA, BLYP, PBE, B3LYP, PBE0, CAM-B3LYP), def2-SVP].

the influence of typical for the intra- and inter-subsystem XC functional as well as for the non-additive kinetic-energy functional in NAKE-based subsystem TDDFT.

As a reference, we first study the corresponding excitation energies and splittings from supermolecular TDDFT. In Fig. 3, we depict the results obtained in these calculations employing various XC functionals. Excitation energies and splittings are shown both for (a) triplet and (b) singlet excitations for inter-subsystem distance in the range from 4.0 to 12.0 Å. As expected for a phenomenon governed by non-electrostatic, short-range effects, the

splitting of the triplet excitation energies is significant only at relatively short inter-subsystem distances, up until 6.0 Å. Within this range, the splittings decrease rapidly with an increasing inter-subsystem separation. The calculated splittings show a clear dependence on the XC functional: The largest splitting (0.14 eV) is obtained with LDA, while GGAs result in splittings between 0.12 eV (BLYP) and 0.11 eV (PBE). Hybrid functionals yield even lower splittings of 0.07 eV (B3LYP), 0.06 eV (PBE0), and 0.05 eV (CAM-B3LYP). Hence, the energy splitting significantly decreases with the amount of exact exchange included in the XC functional used. This behavior was also confirmed for other systems (see Sec. S2 in SI).

For comparison, we also show the corresponding supermolecular results obtained for SEET in Fig. 3b, for which the dependence on the XC approximation is much smaller. Given that SEET is frequently governed by Coulomb interactions, the decrease in splitting occurs less rapidly with increasing distance than for TEET. Furthermore, an asymmetric splitting behavior can be observed for TEET, in contrast to the SEET case. The contribution of the considered SEET transitions are shown in Tab. S3 in the SI.

Turning now to the NAKE-sTDDFT calculations, we first investigated the effect of the intra-subsystem XC functional. Here, LDA,<sup>60</sup> BLYP,<sup>61,62</sup> PBE, B3LYP,<sup>63,64</sup> PBE0, and CAM-B3LYP<sup>65</sup> were considered for inter-subsystem distances between  $R = 3.5$  and 6.5 Å. The results are shown in Fig. 4a.

While the excitation energies at larger distances vary roughly in the range between 4.6 and 5.0 eV for the different intra-subsystem XC functionals, the splittings are very similar and amount to approximately 0.025 eV for the shortest distance investigated here (3.5 Å). In a second step, we tested different combinations of inter-subsystem XC (LDA, PW91) and NAKE (TF, PW91k) functionals. Changing these approximations does lead to changes in the splittings (see Fig. 4b), but even the largest coupling obtained here (0.006 eV at 4.0 Å for PW91/TF) is much smaller than the values obtained in PbE- or supermolecular calculations (see Fig. 3a). Changing from a monomer to a supersystem basis does not lead to significantly different couplings in NAKE-sTDDFT calculations (see Fig. S1 in SI). This



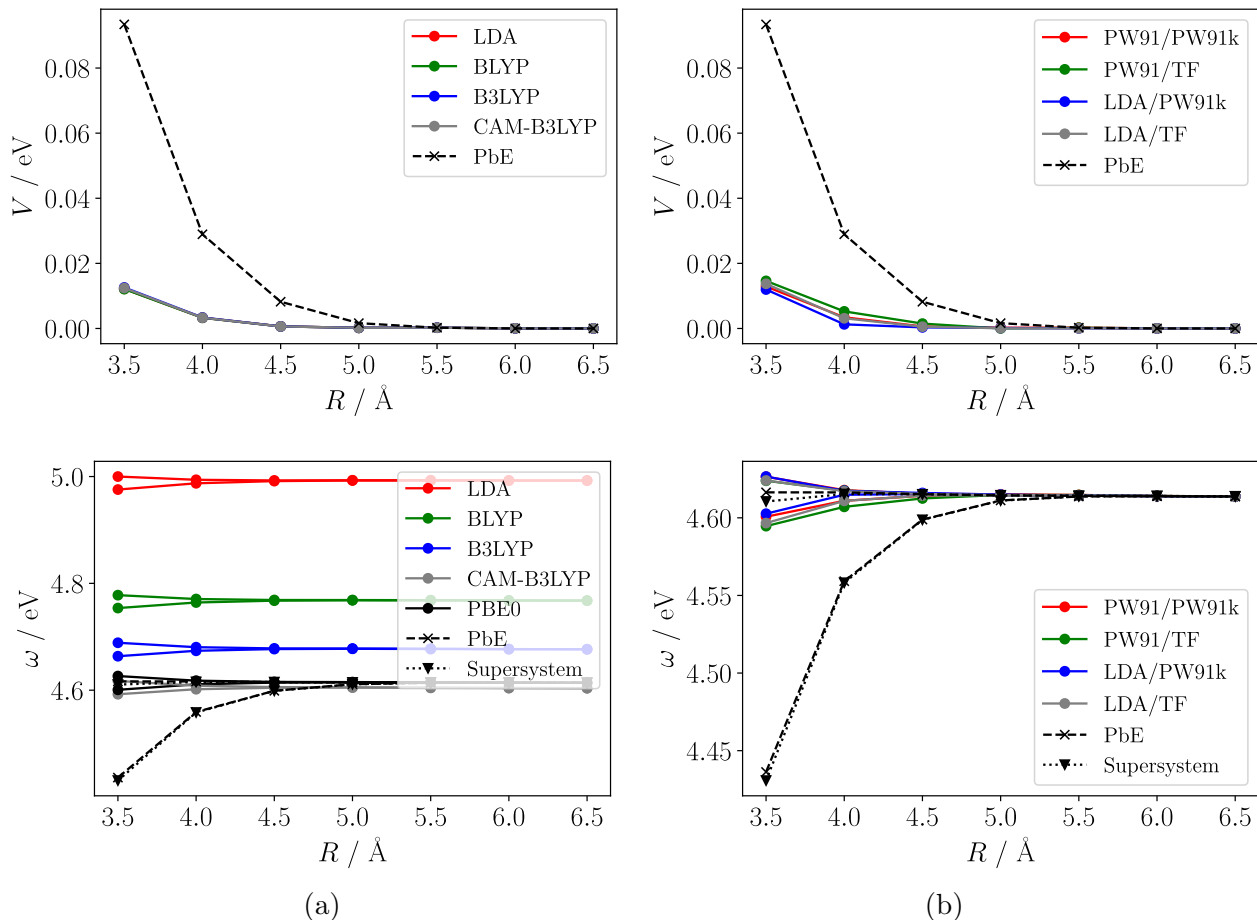


Figure 4: Electronic couplings  $V$  (top) and excitation energies  $\omega$  (bottom) of the  $\pi \rightarrow \pi^*$  triplet excitation of the fluoroethylene dimer as a function of the inter-subsystem separation varying (a) the intra-subsystem [NAKE: (LDA, BLYP, B3LYP, CAM-B3LYP, PBE0)/PW91/PW91k, def2-SVP] and (b) inter-subsystem XC functional dependence [NAKE: PBE0/(PW91, LDA)/(PW91k, TF), def2-SVP] with PbE and supersystem calculations as a reference [PbE: PBE0/PBE0/level.; Supersystem: PBE0, def2-SVP].

shows that with typical approximations as employed here, NAKE-sTDDFT is not well suited for the description of TEET because of the drastic underestimation of the TEET electronic couplings.

## 4.2 PbE-based Subsystem TDDFT for TEET Couplings

While full equivalence to supermolecular results can be achieved with PbE-sTDDFT, this embedding approach also allows for the introduction of approximations regarding the choice of approximate intra- and inter-subsystem XC functionals, as well as variations in the projection

operator (see Sec. S4 in SI). A particular focus will be on the influence of exact exchange. Moreover, an analysis of the different TEET kernel contributions will be carried out to assess their relative importance.

#### 4.2.1 The Role of Exact Exchange

In order to further investigate the origin of the XC functional dependence observed in supermolecular TDDFT, the calculations from Sec. 4.1.2 were repeated using PbE-sTDDFT while varying the XC as well as the non-additive XC functional to differentiate between intra- and inter-subsystem XC approximations. Hence, we examined all combinations of the PBE0 and PBE functionals for the intra- and inter-subsystem interaction to assess how exact exchange affects the electronic couplings and excitation energies of the fluoroethylene dimer. As expected, when consistently varying both XC contributions at the same time, i.e. PBE/PBE or PBE0/PBE0 (see Fig. S2a in the SI), we observe the same changes as in the supermolecular case (cf. Fig. 3). However, changing the amount of exact inter-subsystem exchange does not significantly affect the excitation energies and splittings: As shown in Fig. 5, the results obtained with PBE0/PBE are very similar to the PBE0/PBE0 data. Similarly, the PBE/PBE0 data are very close to the PBE/PBE results (see Fig. S2a in the SI).

These results also demonstrate that exact exchange is not necessary in the inter-subsystem XC approximation to obtain hybrid-functional-quality TEET couplings. This has important consequences on the overall scaling behavior of this approach, as the expensive formal  $n^4$ -scaling when using hybrid functionals can be restricted to the intra-subsystem part.

#### 4.2.2 Separating the Different Kernel Contributions

To gain a deeper understanding of the different contributions to the TEET couplings, we analyzed the individual contributions to the corresponding coupling matrix elements. Assuming the same approximation is used for all intra-subsystem XC functionals and the

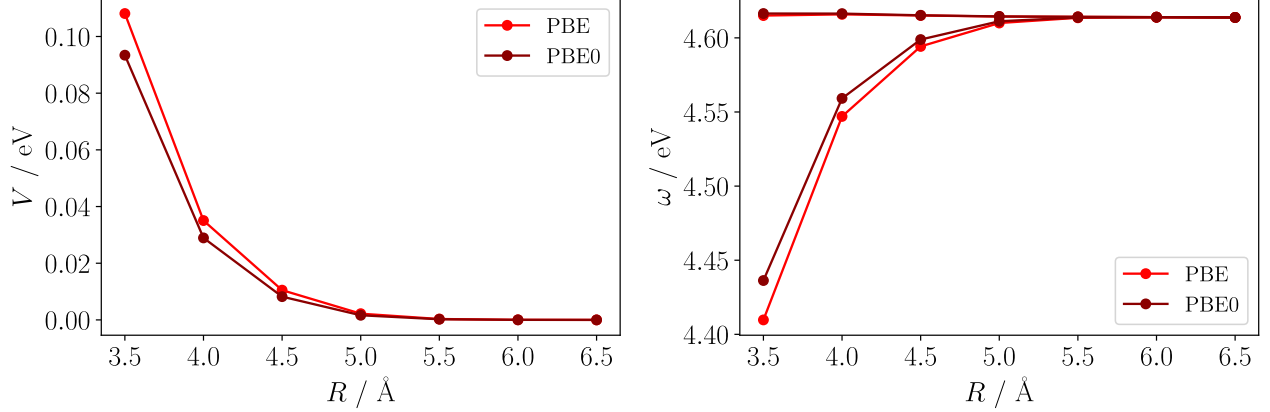


Figure 5: Electronic couplings  $V$  (left) and excitation energies  $\omega$  (right) of the  $\pi \rightarrow \pi^*$  triplet excitation of the fluoroethylene dimer as a function of the inter-subsystem separation with and without exact inter-subsystem exchange [PbE: PBE0/(PBE0, PBE)/level., def2-SVP].

non-additive XC functional, the PbE-sTDDFT triplet coupling matrix using the levelshift operator is defined as

$$K_{(ia)_I, (jb)_J}^{(-), \text{level.}} = (\phi_i^I \phi_a^I | f_{\text{xc}}^{\alpha\alpha} - f_{\text{xc}}^{\alpha\beta} | \phi_j^J \phi_b^J) + c_{\text{HF}} (\phi_i^I \phi_j^J | \phi_a^I \phi_b^J) + \mu \langle \phi_i^I | \phi_j^J \rangle \langle \phi_b^J | \phi_a^I \rangle, \quad (57)$$

where the first part of this equation describes the non-additive XC (NAXC) kernel, the second the exact exchange (XX) kernel, and the third the external-orthogonality (EO) contribution. Fig. 6 presents results obtained with and without the EO kernel contribution. These results reveal that, when considering the EO kernel, the TEET coupling at an inter-subsystem separation of 4.0 Å is approximately 0.03 eV, accompanied by an energy splitting of 0.06 eV. Upon removal of the EO kernel, the electronic coupling virtually vanishes, corresponding to energy splittings close to zero.

The results presented in Fig. 7 provide further evidence for the importance of the EO kernel contributions. In that figure, we show the three different contributions to the TEET couplings identified in Eq. (57) as a function of the amount of exact exchange (both in the intra- and inter-subsystem contributions). It can be seen that the TEET coupling is dominated by the EO kernel independently of the amount of exact exchange, while the NAXC and XX contributions are at least two to three orders of magnitude smaller. Considering that

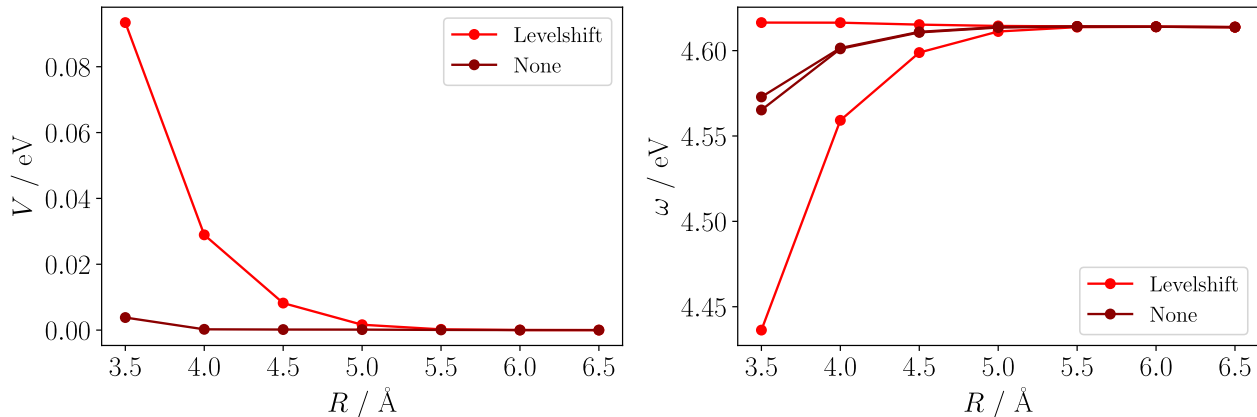


Figure 6: Electronic couplings  $V$  (left) and excitation energies  $\omega$  (right) of the  $\pi \rightarrow \pi^*$  triplet excitation as a function of the inter-subsystem separation of the fluoroethylene dimer with and without considering the EO kernel [PbE: PBE0/PBE0/(level., None), def2-SVP].

the EO kernel depends significantly on the inter-subsystem orbital overlap, the dependence of TEET couplings on the XC functional can most likely be attributed to the orbital topology rather than the inter-subsystem XC approximation. To ensure that the choice of the levelshift parameter  $\mu$  does not influence TEET couplings when using the levelshift operator version of PbE, we systematically varied this parameter in the range of  $10^2$  to  $10^7$ . No significant changes in the electronic couplings could be observed within this parameter range (see Tab. S7 in the SI). Consequently, we can confidently assert that the dependence on the intra-subsystem XC functional is likely related to the topology of the molecular orbitals involved in the transition. A slight decrease of the contribution of the EO kernel, and consequently the TEET coupling kernel can be observed in Fig. 7 as the amount of exact intra-subsystem exchange increases. This can also be attributed to the dependence of the EO kernel on orbital overlap, as a lower amount of exact exchange in the intra-subsystem XC functional leads to less compact and more delocalized molecular orbitals (see, e.g., Refs. 66–69). As a result, the occupied orbitals need to be more strongly localized in the PbE approach, requiring larger orbital rotations to enforce orthogonality of the inter-subsystem orbitals. Therefore, a smaller amount of exact intra-subsystem exchange results in larger TEET couplings.

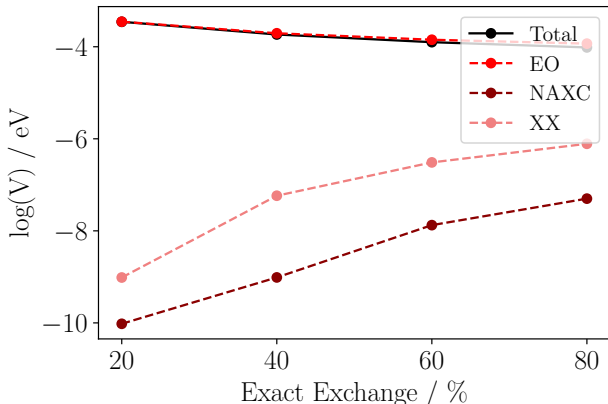


Figure 7: Total electronic coupling  $V$ , as well as contributions of the external-orthogonality (EO), non-additive exchange-correlation (NAXC), and exact exchange (XX) kernel, of the  $\pi \rightarrow \pi^*$  triplet excitation for an inter-subsystem separation of 4.0 Å of the fluoroethylene dimer obtained from PbE-sTDDFT calculations as a function of the amount of exact exchange  $c_{\text{HF}}$  in the intra- and inter-subsystem exchange-correlation functional. PBEx refers to PBE functionals where  $x$  denotes the amount of exact exchange in percent [PbE: PBEx/PBEx/level., def2-SVP].

### 4.3 Application: Investigation of Solvent Effects on TEET Couplings of PDI Dimer Systems

While NAKE-sTDDFT may not be well suited for a proper description of direct TEET couplings as outlined above, it may still be useful to describe explicit solvent effects on TEET in combination with PbE-sTDDFT. Hence, in the following, we will analyze solvent effects on TEET couplings. The mixed PbE-/NAKE-embedding approach introduced in Sec. 2.3, which should be able to take environmental effects into account without compromising accuracy of the direct coupling between the active (PbE-)systems.

As a test system, we choose a (solvated) PDI dimer system. PDI plays an important role in diverse studies concerning potential applications in the field of optoelectronic devices,<sup>70</sup> such as organic solar cells and light-emitting diodes and nanotechnology<sup>71</sup> as well as drug delivery<sup>72</sup> due to its self-assembly behavior. Recently, PDI derivatives have been discussed as possible substituents for fullerenes as the electron acceptor in organic solar cells.<sup>73</sup> Moreover, PDI molecules have been found to exhibit high electron mobility and efficient charge transport

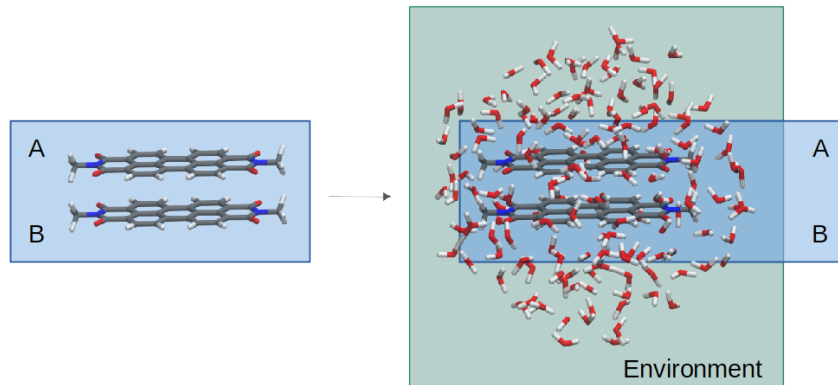


Figure 8: Illustration of the mixed PbE-/NAKE-embedding scheme considering the structure of the PDI dimer surrounded by 149 water molecules, taken from Ref. 50. Description of the PDI dimer using PbE highlighted in blue and the environmental NAKE region highlighted in green.

properties, rendering PDI-based materials promising for organic electronic devices. In addition to its electronic properties, PDI monomers can form a variety of self-assembled structures, including micelles, fibers, and gels. For our purposes, the most important properties of PDI dimer systems are their robustness, modifiable absorption spectrum range, appreciable extinction coefficients, and tendency for strong  $\pi - \pi$  interactions.<sup>74</sup> As such they constitute suitable candidates for benchmarking the different embedding methods for TEET couplings.

#### 4.3.1 Environmental Effect of Explicit Solvent Molecules

As a first test, we investigate the TEET coupling in a solvated PDI dimer with fixed distance as a function of the size of the solvation shell (see Fig. 8). The six lowest-energy  $\pi \rightarrow \pi^*$  triplet excitations of the PDI dimer were determined for an inter-subsystem separation of 3.5 Å, while varying the number of water molecules (see Fig. 9). The selection of water molecules for this purpose was based on the distance from the center of mass of each water molecule to the nearest atom of either of the PDI molecules. The calculations discussed in this subsection were performed with version 1.6.0 of the SERENITY program.<sup>75</sup>

The results presented in Fig. 9 show (a) electronic couplings between the PDI molecules and (b) energy splittings obtained with the mixed PbE-/NAKE-embedding approach, in

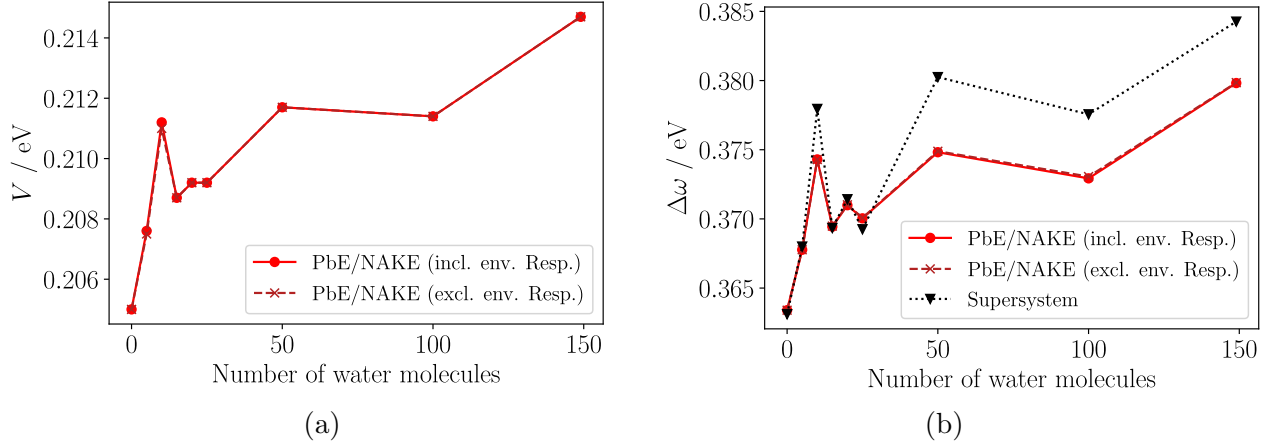


Figure 9: (a) Electronic couplings  $V$  and (b) splittings  $\Delta\omega$  of the  $\pi \rightarrow \pi^*$  triplet excitations for an inter-subsystem separation of 3.5 Å of the PDI dimer in water varying the number of water molecules [Supersystem: PBE0; PbE/NAKE: [PBE0, PBE]/[PBE0, PBE]/[level., PW91K], def2-SVP].

comparison to the corresponding supersystem splittings as a function of the number of water molecules included. In the mixed PbE-/NAKE-embedding calculations, the electronic structures were relaxed in three initial freeze-and-thaw cycles (considering the dimer as a single subsystem). Potentials and kernels in FDE and FDEu calculations for either of the monomers employed a numerical integration grid extending over both molecules (due to the PbE-based description of their interaction). FDE and FDEu calculations for the water molecules used monomer grids and the final FDEc calculation employed a supersystem grid to determine inter-subsystem couplings. For the mixed PbE-/NAKE-embedding approach, we show two sets of data. For the first set, we included *all* response couplings between the PDI molecules (whose interaction is described with PbE) as well as the environmental water molecules (whose interaction is described with NAKE functionals). Within the approximations introduced in the mixed embedding approach, this is equivalent to a supersystem treatment as it includes excitations of and couplings between all subsystems. For the second set, while still including the coupling between the PDI molecules, we neglected the couplings to excitations on the environmental water molecules expecting them to be small. The vacuum supersystem splitting is 0.363 eV which increases to 0.384 eV in the presence of the complete solvation shell containing 149 water molecules. Especially for smaller numbers of water molecules,

this behavior shows some irregularities with intermediate decreases in the splitting as the solvation shell grows. Concerning the PbE/NAKE results, the mixed embedding method qualitatively reproduces the supersystem results, although, for cases involving a larger number of water molecules, there is a deviation of approximately 5 meV. These discrepancies can most likely be traced back to the fact that the response of the solvent molecules is not considered explicitly in this approximate embedding approach. We find no appreciable difference in the electronic couplings computed with the mixed embedding approach, providing evidence that triplet couplings based on NAKE functionals are negligibly small, in line with the findings of previous sections. Therefore, for all subsequent mixed PbE-/NAKE-embedding calculations, the explicit response of the solvent molecules is omitted, leading to a computational advantage. Regarding the TEET couplings acquired through the PbE/NAKE approach, a similar trend emerges in relation to changes in the number of solvent molecules, as observed for the energy splittings. Note that in this system, the TEET electronic couplings are not simply given as half of the energy excitation splitting  $\Delta\omega$ . The reason is that this simple relation does not hold for systems with non-symmetric monomers as is the case here because of the inclusion of explicit solvent molecules. Overall, the environmental effect of the solvent molecules surrounding the chromophores of interest is non-negligible but rather small compared to the total splitting. This is in line with the observations made by Curutchet and Voityuk.<sup>51</sup>

### 4.3.2 Bridge Effect of Explicit Solvent Molecules

In Ref. 51, it turned out that solvent molecules located between the interacting chromophores can more strongly affect the TEET couplings. In the following, we will investigate this aspect in the context of subsystem TDDFT. To this end, we analyze the distance-dependence of TEET couplings in a solvated, stacked PDI dimer in water and two organic solvents of different polarity, namely chloroform (Chl) and benzene (Bnz). In contrast to the example studies above, these structures feature solvent molecules between the PDI monomers, which may enhance the TEET in terms of bridge-mediated effects.<sup>51</sup> The structures of these systems



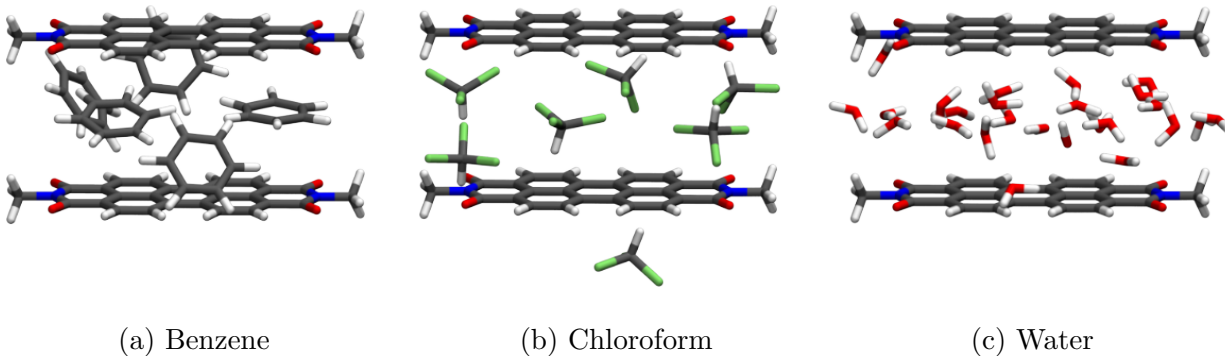


Figure 10: Structures of the PDI dimer with 25 water, seven chloroform, and five benzene molecules in between.

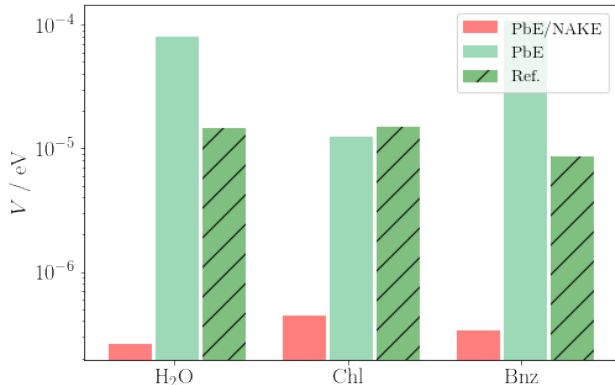


Figure 11: TEET couplings  $V$  at  $R = 7.0 \text{ \AA}$  inter-subsystem separations of the  $\pi \rightarrow \pi^*$  triplet excitations of the PDI dimer in different solvents calculated with mixed PbE-/NAKE-embedding and PbE-sTDDFT with respect to the bridge effect of the solvent molecules [PbE: PBE0/PBE/level.; PbE/NAKE: [PBE0, PBE]/[PBE, PBE]/[level., PW91K], def2-SVP].

were taken from Ref. 51 with inter-subsystem distances of  $R = 7.0$  and  $10.5 \text{ \AA}$ , taking ten snapshots for each solvent and each distance into consideration. Moreover, additional calculations for a PDI–PDI structure with a separation of  $R = 3.5 \text{ \AA}$  were performed to generate reference values for evaluating TEET couplings without bridging solvent molecules.

Initial calculations were performed using mixed PbE-/NAKE-embedding for a fixed inter-subsystem separation of  $R = 7.0 \text{ \AA}$ , corresponding to 25 water, seven chloroform, and five benzene molecules, respectively. Only one snapshot for each solvent was computed (see structures in Fig. 10). As can be seen from Fig. 11, the resulting TEET couplings differ by two orders of magnitude from the reference data of Ref. 51. This shows that the mixed

PbE-/NAKE-embedding is not suitable for describing the bridge-mediated coupling effect of the solvent molecules located in between the chromophores.

For this reason, the response effect of the bridging solvent molecules has to be included explicitly in the description of the electronic couplings using PbE-sTDDFT. This can be achieved by defining two subsystems, each consisting of one chromophore and a certain number of solvent molecules. The latter was determined by calculating the distance from the center of mass of each solvent molecule to the nearest atom of each PDI monomer and subsequently, assigning each of the solvent molecules to one of the monomers based on the solvent–monomer distances. We have also confirmed that different assignments of the solvent molecules to the subsystems only have a minimal effect on the obtained TEET couplings. Including the bridge effect of the solvent molecules in PbE-sTDDFT calculations, TEET couplings at a similar order of magnitude as in Ref. 51 were obtained (see Fig. 11). For instance, when considering 25 water molecules, we determined a TEET coupling of  $8.01 \times 10^{-5}$  eV for the HOMO  $\rightarrow$  LUMO transition of the PDI dimer at  $R = 7.0 \text{ \AA}$ , while Curutchet and Voityuk reported a coupling of  $1.47 \times 10^{-5}$  eV for the same snapshot.<sup>51</sup> It has to be pointed out that Curutchet and Voityuk used the Fragment Excitation Difference (FED) method<sup>76</sup> for computing the couplings, so that some remaining differences can be expected.<sup>77</sup>

### 4.3.3 Conformational Sampling of TEET Couplings

The solvent-mediated coupling strongly depends on the relative orientation of the bridging solvent molecules because of the dependence of TEET couplings on the orbital overlap. Therefore, small changes in the orientation of the solvent or the chromophores can have a large impact on the TEET coupling values. Hence, we calculated the couplings for ten selected chromophore–solvent structures<sup>51</sup> differing in the relative orientation of the solvent molecules in order to provide a more realistic description of the solvent effect. From the data shown in Fig. 12, it can be observed that the average TEET coupling  $\langle V \rangle$  at an inter-subsystem separation of  $R = 10.5 \text{ \AA}$  is around  $10^{-18}$  eV in a vacuum environment. However, when

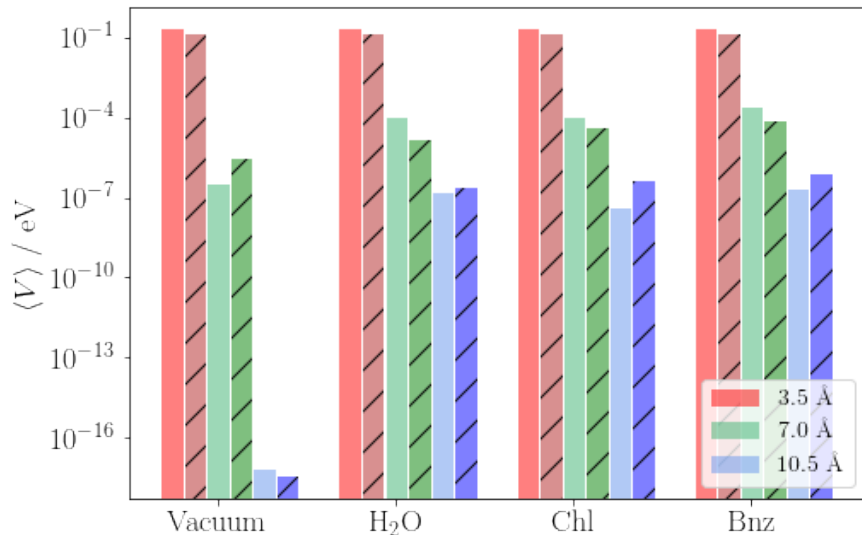


Figure 12: Average TEET couplings  $\langle V \rangle$  at  $R = 3.5, 7.0,$  and  $10.5 \text{ \AA}$  inter-subsystem separations of the  $\pi \rightarrow \pi^*$  triplet excitations of the PDI dimer in benzene, chloroform, and water solutions calculated with PbE-sTDDFT (solid) [PbE: PBE0/PBE/level., def2-SVP], compared to the results in Ref. 51 (striped).

considering the system in solution, the TEET coupling increases to approximately  $10^{-7}$  to  $10^{-8}$  eV for all three solvents considered here, which is qualitatively in agreement with Ref. 51. At an inter-subsystem separation of  $7.0 \text{ \AA}$ , the influence of the solvent leads to an increase of the TEET couplings to about  $10^{-4}$  to  $10^{-5}$  eV, compared to the TEET couplings of roughly  $10^{-7}$  eV in vacuum. In absolute terms, this is a much stronger increase in coupling, while the relative increase is only  $10^3$  compared to an increase of  $10^{11}$  for an inter-subsystem separation of  $10.5 \text{ \AA}$ . These results unambiguously demonstrate that the bridge effect of solvent molecules is crucial when characterizing medium- or long-range TEET processes.

Comparing the calculated couplings for different solvents as shown in Fig. 13, a decrease of the solvent-mediated coupling from benzene via chloroform to water can be observed. Curutchet and Voityuk by contrast observed a reduction in the TEET coupling when going from benzene via chloroform to water. In order to further elucidate the differences between our results and those of Ref. 51, we conducted a recalculation of TEET couplings for ten structures of the PDI dimer system with 25 water molecules located in between and an inter-subsystem distance of  $R = 7.0 \text{ \AA}$  (as illustrated in Fig. 10). We employed the FED approach starting

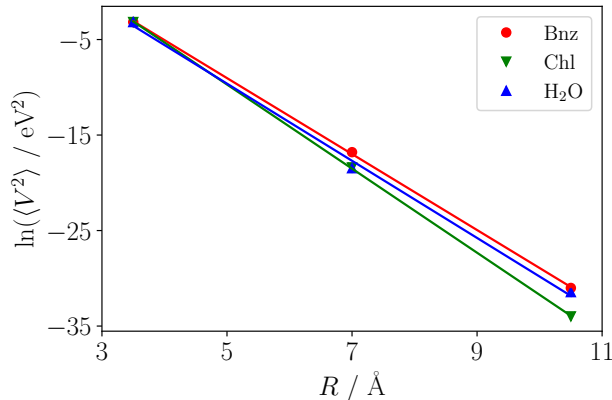


Figure 13: Logarithm of average squared electronic couplings  $\langle V^2 \rangle$  of the  $\pi \rightarrow \pi^*$  triplet excitations of the PDI dimer at  $R = 3.5, 7.0,$  and  $10.5 \text{ \AA}$  inter-subsystem separations in benzene, chloroform, and water solutions calculated with PbE-sTDDFT [PbE: PBE0/PBE/level., def2-SVP].

from TDA [PBE0/def2-SVP] and CIS [HF/def2-SVP] results for determining the electronic couplings and compared the results to both the original data from Ref. 51 [HF/6-31+G(d)] and to our results obtained with PbE-sTDDFT [PBE0/PBE/level., def2-SVP]. The TEET couplings (see Tab. S8 in the SI) from FED based on TDA are in good agreement with PbE-sTDDFT, while FED results based on CIS calculations are in good agreement with the data from Ref. 51. This shows that the discrepancies between our study and Ref. 51 primarily stem from the choice of the electronic structure method (HF vs KS-DFT with PBE0), rather than from the approach used to calculate the TEET couplings (PbE-sTDDFT vs. FED).

## 5 Conclusion

While subsystem Time-Dependent Density-Functional Theory (sTDDFT) based Non-Additive Kinetic Energy (NAKE) functionals is suitable for describing Singlet Excitation-Energy Transfer (SEET), we have demonstrated in this study that it is not well-suited for investigating Triplet Excitation-Energy Transfer (TEET). The energy splittings associated with TEET are severely underestimated when using sTDDFT with approximate NAKE functionals,

deviating significantly from supersystem calculations. Projection-based Embedding (PbE) eliminates these problems and offers a way to directly extract electronic couplings as it acts as a diabaticization scheme. The combination of projection-based embedding with sTDDFT showed promising results for accurately describing TEET processes as long as bridge-mediated TEET is not significant.

A more detailed analysis of the applicability of PbE-sTDDFT for TEET couplings showed that TEET couplings increase as the amount of exact exchange in the XC functional decreases. The functional dependence was found to originate from the intra-subsystem XC functional, while the inter-subsystem XC functional does not have a significant impact on the electronic couplings. We have demonstrated that inter-subsystem exact exchange is not necessary to obtain reliable TEET couplings, and can be replaced by (semi-)local DFT-exchange. This has important consequences when studying TEET couplings in aggregates of coupled chromophores, potentially offering a large performance advantage, as the expensive calculation of exact exchange can be restricted to within the subsystems. A comprehensive study of the composition of the TEET coupling kernel showed that the external-orthogonality (EO) kernel plays a dominant role. As the amount of exact intra-subsystem exchange increases, the significance of the EO kernel, and consequently the TEET coupling kernel, decreases. This can be attributed to the EO kernel's dependence on orbital overlap, as a higher amount of exact exchange in the intra-subsystem XC functional results in more compact and localized molecular orbitals. Hence, it can be assumed that the functional dependence of TEET couplings on the intra-subsystem XC approximation originates from the molecular orbital structure.

The investigation of solvated PDI dimer systems revealed that the mixed PbE-/NAKE-embedding approach introduced in Sec. 2.3 offers the ability to consider environmental effects on TEET between pigments in close contact. However, this approach is no longer applicable if bridge-mediated effects become important. Bridge-mediated TEET can be accurately described by explicitly including the bridging fragments in the PbE-sTDDFT treatment.

Regarding the conformational sampling, our results have shown that while the obtained TEET couplings for different solvents and inter-subsystem separations are comparable to the data in Ref. 51, the observed trend with respect to the solvents is different. Curutchet and Voityuk reported a decrease in electronic couplings from benzene via chloroform to water, while our calculations indicate a decrease from benzene to water to chloroform. We identified the electronic structure method as the origin of these discrepancies (CIS vs. PBE0/PBE), rather than the approach for calculating the TEET couplings: Both PbE-sTDDFT and FED are suitable for calculating TEET couplings in bridge-mediated donor-acceptor systems and yield similar results if the same electronic-structure method is chosen. Subsystem TDDFT can offer an efficiency advantage in this context for more complex and larger systems, as it avoids the need for extensive supersystem calculations. This can pave the way for investigating TEET phenomena in realistic systems as involved in photocatalysis, photovoltaics, and optoelectronic devices, including the effect of a medium surrounding the chromophore groups.

## Acknowledgement

Funding by the Deutsche Forschungsgemeinschaft (DFG, German Research Foundation) through SFB 1459 (Project A03 – 433682494) is gratefully acknowledged. We would like to thank Carles Curutchet for providing the perylene diimide dimer geometries and the data used in Tab. S8 in the SI. J.T. gratefully acknowledges funding by the Deutsche Forschungsgemeinschaft (DFG, German Research Foundation) through DFG-495279997.

## References

- (1) Takiff, L.; Boxer, S. G. Phosphorescence spectra of bacteriochlorophylls. *J. Am. Chem. Soc.* **1988**, *110*, 4425–4426.

- (2) Gust, D.; Moore, T. A.; Moore, A. L. Molecular mimicry of photosynthetic energy and electron transfer. *Acc. Chem. Res.* **1993**, *26*, 198–205.
- (3) Holt, N. E.; Fleming, G. R.; Niyogi, K. K. Toward an Understanding of the Mechanism of Nonphotochemical Quenching in Green Plants. *Biochemistry* **2004**, *43*, 8281–8289.
- (4) Shao, Y.; Yang, Y. Efficient Organic Heterojunction Photovoltaic Cells Based on Triplet Materials. *Adv. Mater.* **2005**, *17*, 2841–2844.
- (5) Luhman, W. A.; Holmes, R. J. Enhanced exciton diffusion in an organic photovoltaic cell by energy transfer using a phosphorescent sensitizer. *Appl. Phys. Lett.* **2009**, *94*, 153304.
- (6) Uoyama, H.; Goushi, K.; Shizu, K.; Nomura, H.; Adachi, C. Highly efficient organic light-emitting diodes from delayed fluorescence. *Nature* **2012**, *492*, 234–238.
- (7) Albin, A. Photosensitization in organic synthesis. *Synthesis* **1981**, *1981*, 249–264.
- (8) Strieth-Kalthoff, F.; James, M. J.; Teders, M.; Pitzer, L.; Glorius, F. Energy transfer catalysis mediated by visible light: principles, applications, directions. *Chem. Soc. Rev.* **2018**, *47*, 7190–7202.
- (9) Zhou, Q.-Q.; Zou, Y.-Q.; Lu, L.-Q.; Xiao, W.-J. Visible-Light-Induced Organic Photochemical Reactions through Energy-Transfer Pathways. *Angew. Chem. Int. Ed.* **2019**, *58*, 1586–1604.
- (10) Strieth-Kalthoff, F.; Glorius, F. Triplet Energy Transfer Photocatalysis: Unlocking the Next Level. *Chem* **2020**, *6*, 1888–1903.
- (11) Neveselý, T.; Wienhold, M.; Molloy, J. J.; Gilmour, R. Advances in the E → Z Isomerization of Alkenes Using Small Molecule Photocatalysts. *Chem. Rev.* **2022**, *122*, 2650–2694.

- (12) Münster, N.; Parker, N. A.; van Dijk, L.; Paton, R. S.; Smith, M. D. Visible Light Photocatalysis of  $6\pi$  Heterocyclization. *Angew. Chem. Int. Ed.* **2017**, *56*, 9468–9472.
- (13) Metternich, J. B.; Gilmour, R. A Bio-Inspired, Catalytic E  $\rightarrow$  Z Isomerization of Activated Olefins. *J. Am. Chem. Soc.* **2015**, *137*, 11254–11257.
- (14) Metternich, J. B.; Gilmour, R. One Photocatalyst, n Activation Modes Strategy for Cascade Catalysis: Emulating Coumarin Biosynthesis with (–)-Riboflavin. *J. Am. Chem. Soc.* **2016**, *138*, 1040–1045.
- (15) Singh, K.; Fennell, C. J.; Coutsiyas, E. A.; Latifi, R.; Hartson, S.; Weaver, J. D. Light harvesting for rapid and selective reactions: click chemistry with strain-loadable alkenes. *Chem* **2018**, *4*, 124–137.
- (16) Teders, M.; Henkel, C.; Anhäuser, L.; Strieth-Kalthoff, F.; Gómez-Suárez, A.; Kleinmans, R.; Kahnt, A.; Rentmeister, A.; Guldi, D.; Glorius, F. The energy-transfer-enabled biocompatible disulfide–ene reaction. *Nature Chemistry* **2018**, *10*, 981–988.
- (17) Welin, E. R.; Le, C.; Arias-Rotondo, D. M.; McCusker, J. K.; MacMillan, D. W. C. Photosensitized, energy transfer-mediated organometallic catalysis through electronically excited nickel(II). *Science* **2017**, *355*, 380–385.
- (18) Dexter, D. L. A Theory of Sensitized Luminescence in Solids. *J. Chem. Phys.* **1953**, *21*, 836–850.
- (19) Lai, R.; Liu, Y.; Luo, X.; Chen, L.; Han, Y.; Lv, M.; Liang, G.; Chen, J.; Zhang, C.; Di, D.; Scholes, G. D.; Castellano, F. N.; Wu, K. Shallow distance-dependent triplet energy migration mediated by endothermic charge-transfer. *Nat. Commun.* **2021**, *12*, 1532.
- (20) Parson, W. W.; Burda, C. *Modern Optical Spectroscopy: From Fundamentals to Appli-*



- cations in Chemistry, Biochemistry and Biophysics*; Springer International Publishing: Cham, 2023; pp 259–279.
- (21) McConnell, H. M. Intramolecular Charge Transfer in Aromatic Free Radicals. *J. Chem. Phys.* **1961**, *35*, 508–515.
- (22) You, Z.-Q.; Hsu, C.-P.; Fleming, G. R. Triplet-triplet energy-transfer coupling: Theory and calculation. *J. Chem. Phys.* **2006**, *124*, 044506.
- (23) Bai, S.; Zhang, P.; Beratan, D. N. Predicting Dexter Energy Transfer Interactions from Molecular Orbital Overlaps. *J. Phys. Chem. C* **2020**, *124*, 18956–18960.
- (24) Casida, M. E.; Wesolowski, T. A. Generalization of the Kohn–Sham equations with constrained electron density formalism and its time-dependent response theory formulation. *Int. J. Quantum Chem.* **2004**, *96*, 577–588.
- (25) Neugebauer, J. Couplings between electronic transitions in a subsystem formulation of time-dependent density functional theory. *J. Phys. Chem.* **2007**, *126*, 134116.
- (26) Böckers, M.; Neugebauer, J. Excitation energies of embedded open-shell systems: Unrestricted frozen-density-embedding time-dependent density-functional theory. *J. Chem. Phys.* **2018**, *149*, 074102.
- (27) Tölle, J.; Böckers, M.; Neugebauer, J. Exact subsystem time-dependent density-functional theory. *J. Chem. Phys.* **2019**, *150*, 181101.
- (28) Wesolowski, T. A.; Warshel, A. Frozen density functional approach for ab initio calculations of solvated molecules. *J. Phys. Chem.* **1993**, *97*, 8050–8053.
- (29) Neugebauer, J.; Veldstra, J.; Buda, F. Theoretical Spectroscopy of Astaxanthin in Crustacyanin Proteins: Absorption, Circular Dichroism, and Nuclear Magnetic Resonance. *J. Phys. Chem. B* **2011**, *115*, 3216–3225.

- (30) König, C.; Neugebauer, J. Protein Effects on the Optical Spectrum of the Fenna–Matthews–Olson Complex from Fully Quantum Chemical Calculations. *J. Chem. Theory Comput.* **2013**, *9*, 1808–1820.
- (31) Eschenbach, P.; Niemeyer, N.; Neugebauer, J. Massively parallel fragment-based quantum chemistry for large molecular systems: the serestipy software. *Can. J. Chem.* **2023**, *101*, 641–655.
- (32) Tölle, J.; Neugebauer, J. The seamless connection of local and collective excited states in subsystem time-dependent density functional theory. *J. Phys. Chem. Lett.* **2022**, *13*, 1003–1018.
- (33) Manby, F. R.; Stella, M.; Goodpaster, J. D.; Miller, T. F. A Simple, Exact Density-Functional-Theory Embedding Scheme. *J. Chem. Theory Comput.* **2012**, *8*, 2564–2568.
- (34) Hégyely, B.; Nagy, P. R.; Ferenczy, G. G.; Kállay, M. Exact density functional and wave function embedding schemes based on orbital localization. *J. Chem. Phys.* **2016**, *145*.
- (35) Wesolowski, T. A.; Weber, J. Kohn-Sham equations with constrained electron density: an iterative evaluation of the ground-state electron density of interacting molecules. *Chem. Phys. Lett.* **1996**, *248*, 71–76.
- (36) Jacob, C. R.; Neugebauer, J. Subsystem density-functional theory. *WIREs Comput. Mol. Sci.* **2014**, *4*, 325–362.
- (37) König, C.; Schlüter, N.; Neugebauer, J. Direct determination of exciton couplings from subsystem time-dependent density-functional theory within the Tamm–Dancoff approximation. *J. Chem. Phys.* **2013**, *138*, 034104.
- (38) Casida, M. E. *Recent Advances In Density Functional Methods: (Part I)*; World Scientific, 1995; pp 155–192.

- (39) Bauernschmitt, R.; Ahlrichs, R. Treatment of electronic excitations within the adiabatic approximation of time dependent density functional theory. *Chem. Phys. Lett.* **1996**, *256*, 454–464.
- (40) Tölle, J.; Böckers, M.; Niemeyer, N.; Neugebauer, J. Inter-subsystem charge-transfer excitations in exact subsystem time-dependent density-functional theory. *J. Chem. Phys.* **2019**, *151*.
- (41) Niemeyer, N.; Tölle, J.; Neugebauer, J. Approximate versus exact embedding for chiroptical properties: Reconsidering failures in potential and response. *J. Chem. Theory Comput.* **2020**, *16*, 3104–3120.
- (42) Hirata, S.; Head-Gordon, M. Time-dependent density functional theory within the Tamm–Dancoff approximation. *Chem. Phys. Lett.* **1999**, *314*, 291–299.
- (43) Huzinaga, S.; Cantu, A. A. Theory of Separability of Many-Electron Systems. *J. Chem. Phys.* **1971**, *55*, 5543–5549.
- (44) Chulhai, D. V.; Jensen, L. External orthogonality in subsystem time-dependent density functional theory. *Phys. Chem. Chem. Phys.* **2016**, *18*, 21032–21039.
- (45) Chulhai, D. V.; Goodpaster, J. D. Projection-based correlated wave function in density functional theory embedding for periodic systems. *J. Chem. Theory Comput.* **2018**, *14*, 1928–1942.
- (46) Tölle, J. *Subsystem-Based Modeling of Photo-Induced Processes*; dissertation, University of Münster, 2021.
- (47) TURBOMOLE V7.5.1, a development of University of Karlsruhe and Forschungszentrum Karlsruhe GmbH, 1989–2007, TURBOMOLE GmbH, since 2007.
- (48) Perdew, J. P.; Burke, K.; Ernzerhof, M. Generalized Gradient Approximation Made Simple. *Phys. Rev. Lett.* **1996**, *77*, 3865.

- (49) Weigend, F.; Ahlrichs, R. Balanced basis sets of split valence, triple zeta valence and quadruple zeta valence quality for H to Rn: Design and assessment of accuracy. *Phys. Chem. Chem. Phys.* **2005**, *7*, 3297–3305.
- (50) Curutchet, C.; Muñoz-Losa, A.; Monti, S.; Kongsted, J.; Scholes, G. D.; Mennucci, B. Electronic Energy Transfer in Condensed Phase Studied by a Polarizable QM/MM Model. *J. Chem. Theory Comput.* **2009**, *5*, 1838–1848.
- (51) Curutchet, C.; Voityuk, A. A. Distance Dependence of Triplet Energy Transfer in Water and Organic Solvents: A QM/MD Study. *J. Phys. Chem. C* **2012**, *116*, 22179–22185.
- (52) Unsleber, J. P.; Dresselhaus, T.; Klahr, K.; Schnieders, D.; Böckers, M.; Barton, D.; Neugebauer, J. Serenity: A Subsystem Quantum Chemistry Program. *J. Comput. Chem.* **2018**, *39*, 788–798.
- (53) Niemeyer, N.; Eschenbach, P.; Bensberg, M.; Tölle, J.; Hellmann, L.; Lampe, L.; Massolle, A.; Rikus, A.; Schnieders, D.; Unsleber, J. P.; Neugebauer, J. The subsystem quantum chemistry program Serenity. *WIREs Computational Molecular Science* **2023**, *13*, e1647.
- (54) Barton, D. et al. qcserenity/serenity: Release 1.5.2. 2023.
- (55) Knizia, G. Intrinsic atomic orbitals: An unbiased bridge between quantum theory and chemical concepts. *J. Chem. Theory Comput.* **2013**, *9*, 4834–4843.
- (56) Perdew, J. P.; Chevary, J. A.; Vosko, S. H.; Jackson, K. A.; Pederson, M. R.; Singh, D. J.; Fiolhais, C. Atoms, molecules, solids, and surfaces: Applications of the generalized gradient approximation for exchange and correlation. *Phys. Rev. B* **1992**, *46*, 6671–6687.
- (57) Lembarki, A.; Chermette, H. Obtaining a gradient-corrected kinetic-energy functional from the Perdew-Wang exchange functional. *Phys. Rev. A* **1994**, *50*, 5328–5331.

- (58) Jacob, C. R.; Beyhan, S. M.; Visscher, L. Exact functional derivative of the nonadditive kinetic-energy bifunctional in the long-distance limit. *J. Chem. Phys.* **2007**, *126*, 234116.
- (59) Scholz, L.; Tölle, J.; Neugebauer, J. Analysis of environment response effects on excitation energies within subsystem-based time-dependent density-functional theory. *Int. J. Quantum Chem.* **2020**, *120*, e26213.
- (60) Vosko, S. H.; Wilk, L.; Nusair, M. Accurate spin-dependent electron liquid correlation energies for local spin density calculations: a critical analysis. *Can. J. Phys.* **1980**, *58*, 1200–1211.
- (61) Becke, A. D. Density-functional exchange-energy approximation with correct asymptotic behavior. *Phys. Rev. A* **1988**, *38*, 3098–3100.
- (62) Lee, C.; Yang, W.; Parr, R. G. Development of the Colle-Salvetti correlation-energy formula into a functional of the electron density. *Phys. Rev. B* **1988**, *37*, 785–789.
- (63) Becke, A. D. Density-functional thermochemistry. III. The role of exact exchange. *J. Chem. Phys.* **1993**, *98*, 5648–5652.
- (64) Stephens, P.; Devlin, F. J.; Chabalowski, C. F.; Frisch, M. J. Ab Initio Calculation of Vibrational Absorption and Circular Dichroism Spectra Using Density Functional Force Fields. *J. Phys. Chem.* **1994**, *98*, 11623–11627.
- (65) Yanai, T.; Tew, D. P.; Handy, N. C. A new hybrid exchange–correlation functional using the Coulomb-attenuating method (CAM-B3LYP). *Chem. Phys. Lett.* **2004**, *393*, 51–57.
- (66) Cohen, A. J.; Mori-Sánchez, P.; Yang, W. Insights into Current Limitations of Density Functional Theory. *Science* **2008**, *321*, 792–794.
- (67) Kim, M.-C.; Sim, E.; Burke, K. Ions in solution: Density corrected density functional theory (DC-DFT). *J. Chem. Phys.* **2014**, *140*, 18A528.

- (68) Vuckovic, S.; Song, S.; Kozlowski, J.; Sim, E.; Burke, K. Density Functional Analysis: The Theory of Density-Corrected DFT. *J. Chem. Theory Comput.* **2019**, *15*, 6636–6646.
- (69) Massolle, A.; Neugebauer, J. Subsystem density-functional theory for interacting open-shell systems: spin densities and magnetic exchange couplings. *Faraday Discuss.* **2020**, *224*, 201–226.
- (70) Kozma, E.; Catellani, M. Perylene diimides based materials for organic solar cells. *Dyes and Pigments* **2013**, *98*, 160–179.
- (71) Kihal, N.; Nazemi, A.; Bourgault, S. Supramolecular Nanostructures Based on Perylene Diimide Bioconjugates: From Self-Assembly to Applications. *Nanomaterials* **2022**, *12*, 1223.
- (72) Zhao, Z.; Xu, N.; Wang, Y.; Ling, G.; Zhang, P. Perylene diimide-based treatment and diagnosis of diseases. *J. Mater. Chem. B* **2021**, *9*, 8937–8950.
- (73) Duan, Y.; Xu, X.; Li, Y.; Peng, Q. Recent development of perylene diimide-based small molecular non-fullerene acceptors in organic solar cells. *Chin. Chem. Lett.* **2017**, *28*, 2105–2115.
- (74) Lin, C.; Kim, T.; Schultz, J. D.; Young, R. M.; Wasielewski, M. R. Accelerating symmetry-breaking charge separation in a perylenediimide trimer through a vibronically coherent dimer intermediate. *Nat. Chem.* **2022**, *14*, 1755–4349.
- (75) Barton, D. et al. qcserenity/serenity: Release 1.6.0. 2023.
- (76) Hsu, C.-P.; You, Z.-Q.; Chen, H.-C. Characterization of the Short-Range Couplings in Excitation Energy Transfer. *J. Phys. Chem. C* **2008**, *112*, 1204–1212.
- (77) Tölle, J.; Cupellini, L.; Mennucci, B.; Neugebauer, J. Electronic couplings for photo-induced processes from subsystem time-dependent density-functional theory: The role of the diabaticization. *J. Chem. Phys.* **2020**, *153*, 184113.

## 6 Appendix

### 6.1 EO Kernel of the Fermi-Shifted Huzinaga Potential

We apply the following definitions for notational brevity in the following:

$$F_{\mu\nu}^{IJ} = \langle \chi_{\mu}^I | \hat{F} | \chi_{\nu}^J \rangle, \quad (58)$$

$$S_{\mu\nu}^{IJ} = \langle \chi_{\mu}^I | \chi_{\nu}^J \rangle, \quad (59)$$

where  $I$  and  $J$  label subsystems,  $\hat{F}$  is the supersystem Fock operator, and  $\chi$  are basis functions, which can, but need not necessarily, belong to the same supermolecular basis set. The Fermi-shifted Huzinaga potential<sup>45</sup> in the atomic-orbital basis of subsystem  $A$  in the presence of another subsystem  $B$  reads:

$$V_{\mu\nu}^{\text{Fermi},A(B)} = - \sum_{\kappa\lambda} (F_{\mu\kappa}^{AB} - \epsilon_F S_{\mu\kappa}^{AB}) D_{\kappa\lambda}^B S_{\lambda\nu}^{BA} - \sum_{\kappa\lambda} S_{\mu\kappa}^{AB} D_{\kappa\lambda}^B (F_{\lambda\nu}^{BA} - \epsilon_F S_{\lambda\nu}^{BA}) \quad (60)$$

$$= - \sum_{\kappa\lambda} F_{\mu\kappa}^{AB} D_{\kappa\lambda}^B S_{\lambda\nu}^{BA} - \sum_{\kappa\lambda} S_{\mu\kappa}^{AB} D_{\kappa\lambda}^B F_{\lambda\nu}^{BA} + 2\epsilon_F \sum_{\kappa\lambda} S_{\mu\kappa}^{AB} D_{\kappa\lambda}^B S_{\lambda\nu}^{BA} \quad (61)$$

$$= V_{\mu\nu}^{\text{Huz.},A(B)} + 2\epsilon_F \sum_{\kappa\lambda} S_{\mu\kappa}^{AB} D_{\kappa\lambda}^B S_{\lambda\nu}^{BA}, \quad (62)$$

where the first two summands are equivalent to the regular Huzinaga potential<sup>34</sup> and the second one resembles the potential arising from the use of the levelshift operator<sup>33</sup> scaled with the Fermi shift  $\epsilon_F$ . To obtain an expression of the corresponding coupling-matrix contributions of  $V_{\mu\nu}^{\text{Fermi},A(B)}$ , we first rewrite the density matrix of  $B$  in the molecular-orbital representation,

$$D_{\kappa\lambda}^B = \sum_{(pq)_B} C_{\kappa p}^B D_{pq}^B C_{\lambda q}^B \quad (63)$$

and transform the whole expression to the molecular-orbital basis of  $A$

$$V_{ia}^{\text{Fermi},A(B)} = \sum_{\mu\nu} C_{\mu i}^A V_{\mu\nu}^{\text{Fermi},A(B)} C_{\nu a}^A \quad (64)$$

$$= - \sum_{(pq)_B} F_{ip}^{AB} D_{pq}^B S_{qa}^{BA} - \sum_{(pq)_B} S_{ip}^{AB} D_{pq}^B F_{qa}^{BA} + 2\epsilon_F \sum_{(pq)_B} S_{ip}^{AB} D_{pq}^B S_{qa}^{BA} \quad (65)$$

$$= V_{ia}^{\text{Huz.},A(B)} + 2\epsilon_F \sum_{(pq)_B} S_{ip}^{AB} D_{pq}^B S_{qa}^{BA}. \quad (66)$$

The external-orthogonality kernel of the Fermi-Shifted Huzinaga operator is then obtained as

$$K_{(ia)_A,(jb)_B}^{\text{Fermi},A(B)} = \frac{\partial V_{ia}^{\text{Fermi},A(B)}}{\partial D_{jb}^B} \quad (67)$$

$$= K_{(ia)_A,(jb)_B}^{\text{Huz.},A(B)} + 2\epsilon_F S_{ij}^{AB} S_{ba}^{BA}, \quad (68)$$

where the contribution beyond the regular Huzinaga kernel<sup>40</sup> (which, in turn, resembles the levelshift kernel contribution<sup>27</sup>) may become non-negligible if no supersystem basis set is used (which would imply that  $S_{ij}^{AB} = S_{ba}^{BA} = 0$ ). We, therefore, explicitly include it in calculations with the Fermi-shifted Huzinaga operator.



# Triplet Excitation-Energy Transfer Couplings from Subsystem Time-Dependent Density-Functional Theory

– Supporting Information –

Sabine Käfer<sup>1</sup>, Niklas Niemeyer<sup>1</sup>, Johannes Tölle<sup>2</sup>, and Johannes  
Neugebauer<sup>1,\*</sup>

<sup>1</sup>University of Münster, Organisch-Chemisches Institut  
and Center for Multiscale Theory and Computation,  
Corrensstraße 36, 48149 Münster, Germany

<sup>2</sup>Division of Chemistry and Chemical Engineering,  
California Institute of Technology, Pasadena, California 91125, USA

Date: December 12, 2023

---

\*email: j.neugebauer@uni-muenster.de

# S1 Dominant Orbital Transitions

## a) Helium Dimer

**Table S1:** Excitation energies  $\omega$  and dominant orbital transitions of the four lowest-lying triplet excitations of the helium dimer at 1.0 Å separation, corresponding to the HOMO  $\rightarrow$  LUMO local excitation (LE) and charge-transfer (CT) transitions.

State	$\omega$ / eV	System	Type	Dominant orbital transition
T <sub>1</sub>	37.71	1	LE	HOMO $\rightarrow$ LUMO (31.35%)
		2	LE	HOMO $\rightarrow$ LUMO (31.35%)
		1	CT	HOMO $\rightarrow$ LUMO (18.65%)
		2	CT	HOMO $\rightarrow$ LUMO (18.65%)
T <sub>2</sub>	39.19	1	LE	HOMO $\rightarrow$ LUMO (33.24%)
		2	LE	HOMO $\rightarrow$ LUMO (33.24%)
		1	CT	HOMO $\rightarrow$ LUMO (16.76%)
		2	CT	HOMO $\rightarrow$ LUMO (16.76%)
T <sub>3</sub>	49.25	1	CT	HOMO $\rightarrow$ LUMO (33.24%)
		2	CT	HOMO $\rightarrow$ LUMO (33.24%)
		1	LE	HOMO $\rightarrow$ LUMO (16.76%)
		2	LE	HOMO $\rightarrow$ LUMO (16.76%)
T <sub>4</sub>	50.49	1	CT	HOMO $\rightarrow$ LUMO (31.35%)
		2	CT	HOMO $\rightarrow$ LUMO (31.35%)
		1	LE	HOMO $\rightarrow$ LUMO (18.65%)
		2	LE	HOMO $\rightarrow$ LUMO (18.65%)

**Table S2:** Excitation energies  $\omega$  and dominant orbital transitions of the four lowest-lying singlet excitations of the helium dimer at 1.0 Å separation, corresponding to the HOMO  $\rightarrow$  LUMO local excitation (LE) and charge-transfer (CT) transitions.

State	$\omega$ / eV	System	Type	Dominant orbital transition
S <sub>1</sub>	43.25	1	CT	HOMO $\rightarrow$ LUMO (40.15%)
		2	CT	HOMO $\rightarrow$ LUMO (40.15%)
		1	LE	HOMO $\rightarrow$ LUMO ( 9.85%)
		2	LE	HOMO $\rightarrow$ LUMO ( 9.85%)
S <sub>2</sub>	43.95	2	CT	HOMO $\rightarrow$ LUMO (41.17%)
		1	CT	HOMO $\rightarrow$ LUMO (41.17%)
		1	LE	HOMO $\rightarrow$ LUMO ( 8.83%)
		2	LE	HOMO $\rightarrow$ LUMO ( 8.83%)
S <sub>3</sub>	55.44	1	LE	HOMO $\rightarrow$ LUMO (41.17%)
		2	LE	HOMO $\rightarrow$ LUMO (41.17%)
		1	CT	HOMO $\rightarrow$ LUMO ( 8.83%)
		2	CT	HOMO $\rightarrow$ LUMO ( 8.83%)
S <sub>4</sub>	57.26	2	LE	HOMO $\rightarrow$ LUMO (40.15%)
		1	LE	HOMO $\rightarrow$ LUMO (40.15%)
		1	CT	HOMO $\rightarrow$ LUMO ( 9.85%)
		2	CT	HOMO $\rightarrow$ LUMO ( 9.85%)

## b) Fluoroethylene Dimer

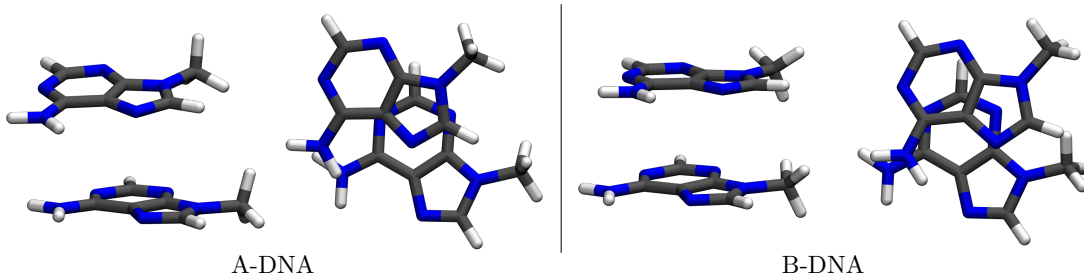
**Table S3:** Excitation energies  $\omega$  and dominant orbital transitions of the four lowest-lying triplet excitations of the fluoroethylene dimer at 4.0 Å separation, corresponding to the HOMO  $\rightarrow$  LUMO local excitation (LE) and charge-transfer (CT) transitions.

State	$\omega$ / eV	System	Type	Dominant orbital transition
T <sub>1</sub>	4.56	2	LE	HOMO $\rightarrow$ LUMO (48.57%)
		1	LE	HOMO $\rightarrow$ LUMO (48.56%)
T <sub>2</sub>	4.62	1	LE	HOMO $\rightarrow$ LUMO (49.62%)
		2	LE	HOMO $\rightarrow$ LUMO (49.62%)
T <sub>3</sub>	7.19	1	CT	HOMO $\rightarrow$ LUMO (49.99%)
		2	CT	HOMO $\rightarrow$ LUMO (49.99%)
T <sub>4</sub>	7.26	2	CT	HOMO $\rightarrow$ LUMO (48.93%)
		1	CT	HOMO $\rightarrow$ LUMO (48.92%)

## S2 Dependence of TEET Couplings on Intra- and Inter-Subsystem XC Approximations

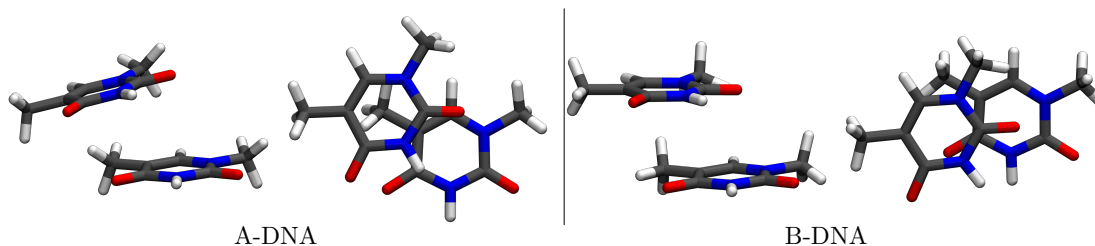
### a) DNA Base Pairs

**Table S4:** Excitation energies  $\omega$  (in eV) and splittings  $\Delta\omega$  (in eV) of the  $\pi \rightarrow \pi^*$  triplet excitation of the stacked adenine–adenine DNA base pair in A- and B-DNA obtained from supersystem calculations with different exchange–correlation functionals. Two excitation energies are given because of the splitting of triplet excitations. Side (left) and front (right) view of stacked A–A DNA bases in A- and B-DNA [Supersystem: (LDA, BLYP, PBE, B3LYP, PBE0, CAM-B3LYP), def2-SVP].



	XC Functional					
	LDA	BLYP	PBE	B3LYP	PBE0	CAM-B3LYP
<b>A-DNA</b>						
$\omega$	3.62766	3.58628	3.59648	3.79983	3.83253	3.93740
	3.72505	3.65340	3.66270	3.82437	3.85131	3.94868
$\Delta\omega$	0.09739	0.06712	0.06622	0.02454	0.01878	0.01128
<b>B-DNA</b>						
$\omega$	3.71373	3.64155	3.65195	3.81453	3.84312	3.94336
	3.75848	3.67793	3.68842	3.84303	3.86979	3.96660
$\Delta\omega$	0.04475	0.03638	0.03647	0.02850	0.02667	0.02324

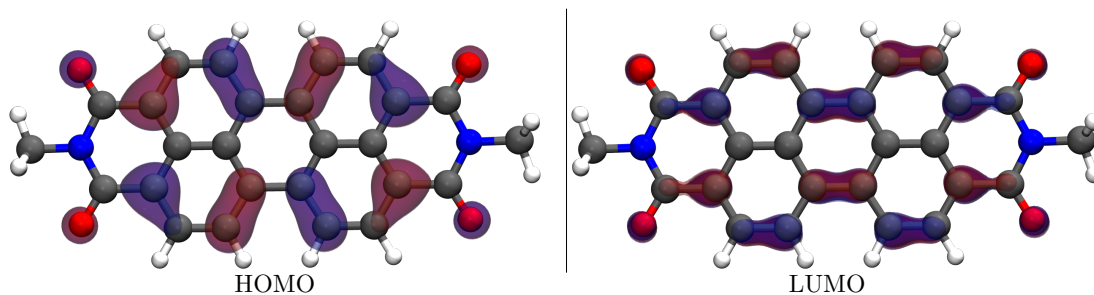
**Table S5:** Excitation energies  $\omega$  (in eV) and splittings  $\Delta\omega$  (in eV) of the  $\pi \rightarrow \pi^*$  triplet excitation of the stacked thymine–thymine DNA base pair in A- and B-DNA obtained from supersystem calculations with different exchange–correlation functionals. Two excitation energies are given because of the splitting of triplet excitations. Side (left) and front (right) view of stacked T–T DNA bases in A- and B-DNA [Supersystem: (LDA, BLYP, PBE, B3LYP, PBE0, CAM-B3LYP), def2-SVP].



	XC Functional					
	LDA	BLYP	PBE	B3LYP	PBE0	CAM-B3LYP
<b>A-DNA</b>						
$\omega$	3.20229	3.18666	3.17333	3.29501	3.28174	3.33011
	3.35610	3.30850	3.30172	3.40828	3.40349	3.45178
$\Delta\omega$	0.15381	0.12184	0.12839	0.11327	0.12175	0.12167
<b>B-DNA</b>						
$\omega$	3.17229	3.12597	3.12383	3.21472	3.21053	3.24955
	3.24505	3.18026	3.17673	3.24457	3.23372	3.26865
$\Delta\omega$	0.07276	0.05429	0.05290	0.02985	0.02319	0.01910

## b) PDI Dimer

**Table S6:** Excitation energies  $\omega$  (in eV) and splittings  $\Delta\omega$  (in eV) of the  $\pi \rightarrow \pi^*$  triplet excitation of the PDI dimer for an inter-subsystem separation of 3.5 Å obtained from super-system calculations with different exchange–correlation functionals. Two excitation energies are given because of the splitting of triplet excitations. HOMO and LUMO of a PDI monomer are shown [Supersystem: (LDA, BLYP, PBE, B3LYP, PBE0, CAM-B3LYP), def2-SVP].



	XC Functional					
	LDA	BLYP	PBE	B3LYP	PBE0	CAM-B3LYP
$\omega$	0.87110	0.87167	0.87701	1.03143	1.05993	1.25130
	1.36873	1.32854	1.32680	1.41848	1.42304	1.54866
$\Delta\omega$	0.49763	0.45687	0.44979	0.38705	0.36311	0.29736

### S3 Dependence of TEET Couplings on the Basis in NAKE-sTDDFT Calculations

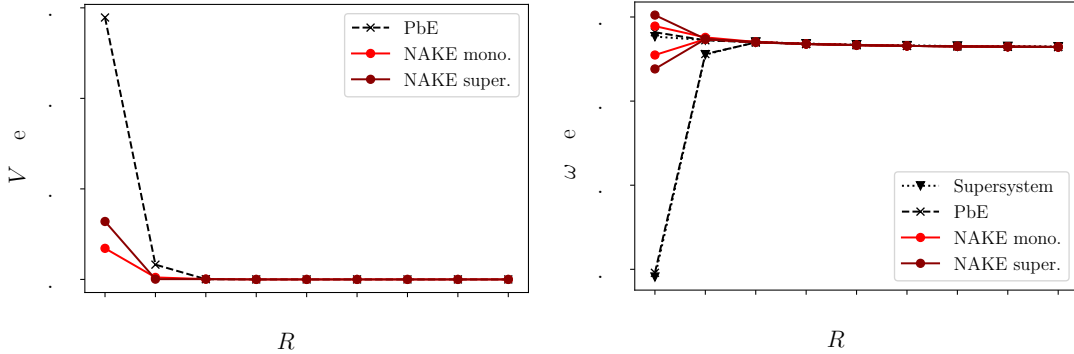


**Figure S1:** Electronic couplings  $V$  (left) and excitation energies  $\omega$  (right) of the  $\pi \rightarrow \pi^*$  triplet excitation as a function of the inter-subsystem separation of the fluoroethylene dimer [PbE: PBE0/PBE0/level.; NAKE: PBE0/PW91/PW91k; Supersystem: PBE0, def2-SVP].

### S4 Influence of the Projection Operator

As another aspect, the influence of the selected projection operator on the resulting TEET couplings was explored. In addition to the levelshift operator applied in all PbE calculations presented above, we also test the Huzinaga operator in the following. In contrast to the levelshift operator, the Huzinaga operator contains contributions from the Fock matrix and may hence show a more intricate dependence on the inter-subsystem XC approximation.

In Fig. S2, electronic couplings and excitation energies for the fluoroethylene dimer system and using different combinations of the PBE0 and PBE as the intra- and inter-subsystem XC functional and the def2-SVP basis set were determined employing either the levelshift or the Huzinaga operator. The results obtained are very similar for the two projection operators, which holds both for functionals with (PBE0) and without (PBE) exact exchange contributions. Additional investigations were carried out concerning the dependence of the Fock matrix contributions within the Huzinaga kernel. Also for these contributions, it turns out that exact inter-subsystem exchange is not needed in order to obtain accurate results. This shows that there is no distinct advantage of the levelshift operator in terms of the dependence on the XC approximations.

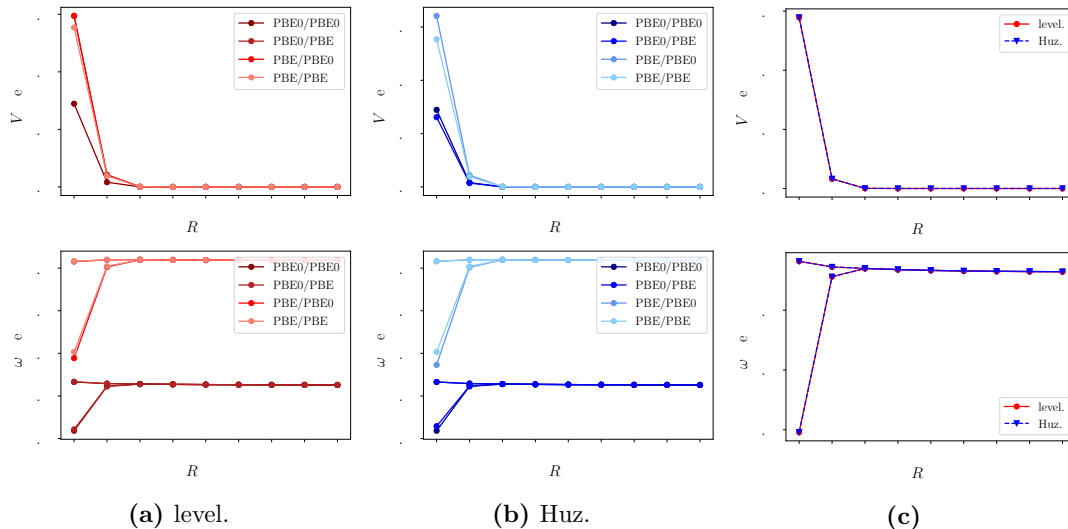


**Figure S2:** Electronic couplings (top) and excitation energies (bottom) of the  $\pi \rightarrow \pi^*$  triplet excitation as a function of the inter-subsystem separation of the fluoroethylene dimer obtained from PbE-sTDDFT using the (a) levelshift and (b) Huzinaga projection operator [PbE: (PBE0, PBE)/(PBE0, PBE)/(level., Huz.), def2-SVP], as well as (c) a direct comparison of both projectors [PbE: PBE0/PBE0/(level., Huz.), def2-SVP].

**Table S7:** Impact of the levelshift parameter  $\mu$  on the electronic coupling  $V$  and excitation energies  $\omega$  of the HOMO  $\rightarrow$  LUMO excitation of the fluoroethylene dimer for an inter-subsystem separation of 4.0 Å obtained from PbE-sTDDFT calculations [PbE: PBE0/PBE0/level., def2-SVP].

$\mu$	$V / \text{eV}$	$\omega_1 / \text{eV}$	$\omega_2 / \text{eV}$
$10^2$	0.02893	4.55919	4.61637
$10^3$	0.02893	4.55917	4.61637
$10^4$	0.02893	4.55917	4.61637
$10^5$	0.02893	4.55917	4.61637
$10^6$	0.02893	4.55917	4.61637
$10^7$	0.02893	4.55917	4.61637



## S5 Dependence of Bridge-Mediated TEET Couplings on the Number of Solvent Molecules

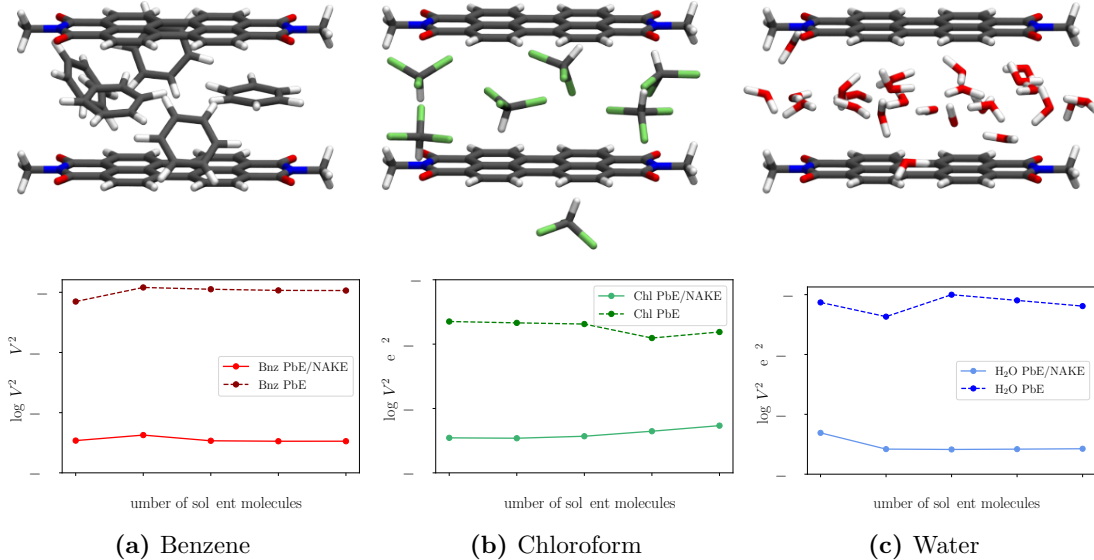


**Figure S3:** Dependence of the logarithm of squared TEET couplings  $V^2$  at  $R = 7.0 \text{ \AA}$  inter-subsystem separations of the  $\pi \rightarrow \pi^*$  triplet excitation of the PDI dimer on the number of solvent molecules included in the model using water, chloroform (Chl), and benzene (Bnz) calculated with mixed PbE-/NAKE-embedding and PbE-sTDDFT [PbE: PBE0/PBE/level.; PbE/NAKE: [PBE0, PBE]/[PBE, PBE]/[level., PW91k], def2-SVP].

Based on structures provided by Carles Curutchet and used in Ref. [1], we systematically investigated the dependence of bridge-mediated couplings on the number of bridging solvent molecules, following a similar approach. For the sake of completeness, Fig. S3 shows squared electronic couplings for increasing numbers of solvent molecules of one PDI dimer snapshot in different solvents ( $R = 7.0 \text{ \AA}$ ). Apparently, changing the number of solvent molecules has only a minor effect on the TEET couplings for the various solvents once a certain minimal number of solvent molecules is included. Note that we employ the structures provided by Carles Curutchet and used in Ref. [1] without further modifications. These calculations were only conducted for the purpose of comparing our method for describing TEET couplings with the literature.

# S6 Comparison of Bridge-Mediated TEET Couplings from the Fragment Excitation Difference Method and Subsystem TDDFT

**Table S8:** TEET couplings  $V$  (in eV) at  $R = 7.0$  Å inter-subsystem separations of the  $\pi \rightarrow \pi^*$  triplet excitations of the PDI dimer with 25 water molecules located in between calculated with PbE-sTDDFT [PBE0/PBE/level., def2-SVP] and the Fragment Excitation Difference (FED) method on the basis of TDA [PBE0/def2-SVP] and CIS calculations [HF/def2-SVP], compared to data obtained in Ref. [1] [HF/6-31+G(d)].

System	PbE-sTDDFT	FED/TDA	FED/CIS	Ref.
1	$8.01 \times 10^{-5}$	$8.23 \times 10^{-5}$	$1.32 \times 10^{-5}$	$1.47 \times 10^{-5}$
2	$1.25 \times 10^{-4}$	$1.31 \times 10^{-4}$	$1.64 \times 10^{-5}$	$1.65 \times 10^{-5}$
3	$8.30 \times 10^{-5}$	$8.92 \times 10^{-5}$	$1.02 \times 10^{-5}$	$1.03 \times 10^{-5}$
4	$7.04 \times 10^{-5}$	$7.14 \times 10^{-5}$	$8.01 \times 10^{-6}$	$9.40 \times 10^{-6}$
5	$1.51 \times 10^{-4}$	$1.63 \times 10^{-4}$	$1.97 \times 10^{-5}$	$1.93 \times 10^{-5}$
6	$3.94 \times 10^{-5}$	$3.96 \times 10^{-5}$	$2.18 \times 10^{-6}$	$3.04 \times 10^{-6}$
7	$1.46 \times 10^{-4}$	$1.50 \times 10^{-4}$	$1.37 \times 10^{-5}$	$1.19 \times 10^{-5}$
8	$1.69 \times 10^{-5}$	$1.77 \times 10^{-5}$	$1.84 \times 10^{-6}$	$1.53 \times 10^{-6}$
9	$3.43 \times 10^{-5}$	$3.43 \times 10^{-5}$	$3.38 \times 10^{-6}$	$2.18 \times 10^{-6}$
10	$2.29 \times 10^{-4}$	$2.39 \times 10^{-4}$	$2.59 \times 10^{-5}$	$2.54 \times 10^{-5}$

## References

- [1] C. Curutchet, A. A. Voityuk, *J. Phys. Chem. C* **2012**, *116*, 22179–22185.